Quantitative interactomics in primary T cells unveils TCR signal diversification extent and dynamics

Guillaume Voisinne, Kristof Kersse, Karima Chaoui, Liaoxun Lu, Julie Chaix, Lichen Zhang, Marisa Goncalves Menoita, Laura Girard, Youcef Ounoughene, Hui Wang, et al.

RESOURCE
https://doi.org/10.1038/s41590-019-0489-8
nature immunology

Quantitative interactomics in primary T cells unveils TCR signal diversification extent and dynamics

Guillaume Voisinne[1], Kristof Kersse[1], Karima Chaoui[2], Liaoxun Lu[3,4], Julie Chaix[1], Lichen Zhang[3], Marisa Goncalves Menoita[1], Laura Girard[1,5], Youcef Ounoughene[1], Hui Wang[3], Odile Burlet-Schiltz[2], Hervé Luche[5,6], Frédéric Fiore[5], Marie Malissen[1,5,6], Anne Gonzalez de Peredo[2], Yinming Liang[3,6*], Romain Roncagalli[1*] and Bernard Malissen[1,5,6*]

The activation of T cells by the T cell antigen receptor (TCR) results in the formation of signaling protein complexes (signalosomes), the composition of which has not been analyzed at a systems level. Here, we isolated primary CD4$^+$ T cells from 15 gene-targeted mice, each expressing one tagged form of a canonical protein of the TCR-signaling pathway. Using affinity purification coupled with mass spectrometry, we analyzed the composition and dynamics of the signalosomes assembling around each of the tagged proteins over 600 s of TCR engagement. We showed that the TCR signal-transduction network comprises at least 277 unique proteins involved in 366 high-confidence interactions, and that TCR signals diversify extensively at the level of the plasma membrane. Integrating the cellular abundance of the interacting proteins and their interaction stoichiometry provided a quantitative and contextual view of each documented interaction, permitting anticipation of whether ablation of a single interacting protein can impinge on the whole TCR signal-transduction network.

T cells express TCRs on their surface, through which they detect antigens. The initiation of TCR signals relies on the LCK and ZAP70 protein tyrosine kinases (PTKs) and generates protein assemblages of considerable complexity[1–3]. Most previous approaches aiming at disentangling such complexity addressed one protein at a time, with limited quantitative insight. As a result, it remains difficult to understand how the TCR signal-transduction network processes signals and to predict the effects resulting from a mutation or a drug.

Affinity purification of a protein of interest (the 'bait') with its interacting partners (the 'preys'), coupled with mass spectrometry (AP–MS), permits the definition of the composition of the corresponding protein complex as a set of binary bait–prey interactions, termed an 'interactome'. We provided proof-of-concept for interactomics in primary CD4$^+$ T cells by determining the composition of the multiprotein complexes that formed around ZAP70 and the adaptors LAT and SLP-76 (ref. [4]). However, that pilot study was limited to three baits and relied on pervanadate-based T cell activation, a stimulation condition that is less physiological than that resulting from engagement of the TCR in combination with CD4 or CD8 coreceptors. Here, we extended our interactomics approach to signaling complexes ('signalosomes') that assemble around 15 canonical proteins used by the proximal TCR signal-transduction network. We avoided the pitfalls associated with transformed T cells[5] by using primary CD4$^+$ T cells, and we captured signaling dynamics by analyzing each of the 15 signalosomes before and at four different time points after anti-TCR plus anti-CD4 stimulation. A total of 277 unique proteins involved in 366 high-confidence protein–protein interactions (PPIs) were identified within the proximal TCR signal-transduction network, a complexity that led us to revisit the mode of action of several signalosomes used by the TCR.

TCR signals are classically described as proceeding from the TCR to the inside of T cells via the LAT transmembrane adaptor, which is thought to serve as the earliest and often sole point of signal diversification downstream of the TCR[2]. In our original interactomics study, we showed that the transmembrane receptor CD6 was also able to nucleate its own signalosome in response to TCR signaling, and independently of LAT[4]. However, the lack of information on the numbers of complexes nucleating around LAT and CD6 precluded assessing their respective quantitative contribution to early TCR signal propagation and diversification. Here, by capitalizing on the recent possibilities to measure both the numbers of copies per cell (cellular protein abundance) of each interacting protein, and the quantitative relationship existing between a bait and a prey in a given complex (interaction stoichiometry)[6], we succeeded in identifying and quantifying the TCR-inducible signalosomes that form at the inner face of the plasma membrane. Unexpectedly, the CD5 and CD6 transmembrane receptors assembled signalosomes with kinetics and in numbers comparable to those nucleated by the LAT adaptor, demonstrating that the breadth of early TCR signal diversification is larger than expected. Finally, to decipher the function of the poorly characterized interacting proteins identified within the

[1]Centre d'Immunologie de Marseille-Luminy, Aix Marseille Université, INSERM, CNRS, Marseille, France. [2]Institut de Pharmacologie et de Biologie Structurale, Département Biologie Structurale Biophysique, Protéomique Génopole Toulouse Midi Pyrénées CNRS UMR 5089, Toulouse, France. [3]School of Laboratory Medicine, Xinxiang Medical University, Xinxiang, China. [4]Laboratory of Mouse Genetics, Institute of Psychiatry and Neuroscience, Xinxiang Medical University, Xinxiang, China. [5]Centre d'Immunophénomique, Aix Marseille Université, INSERM, CNRS UMR, Marseille, France. [6]Laboratory of Immunophenomics, School of Laboratory Medicine, Xinxiang Medical University, Xinxiang, China. *e-mail: yinming.liang@foxmail.com; roncagalli@ciml.univ-mrs.fr; bernardm@ciml.univ-mrs.fr

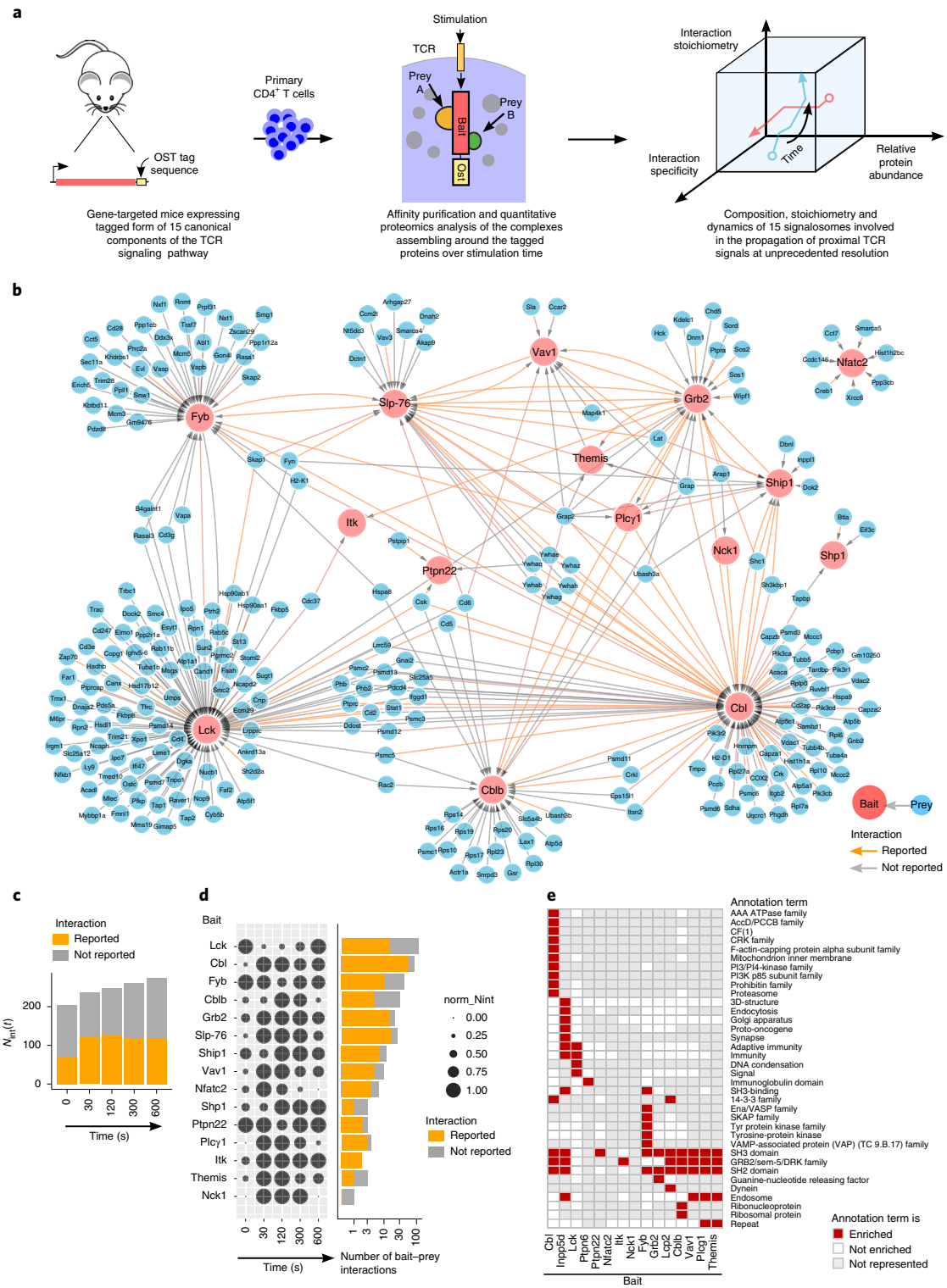

Fig. 1 | Composition of the protein–protein network assembling around 15 canonical proteins of the TCR-signaling pathway over 600 s of stimulation. **a**, Workflow schematic for mapping the composition, stoichiometry and dynamics of the signaling complexes assembling around 15 canonical proteins of the TCR-signaling network of primary CD4+ T cells before and after TCR activation for 30, 120, 300 and 600 s. **b**, High-confidence interactome forming around the 15 baits. High-confidence bait–prey interactions were defined as having an FDR value ≤3% for two consecutive time points of stimulation (see 'Statistics and data reproducibility' in Methods). OST-tagged baits and preys are represented in red and blue, respectively. Interactions already reported in databases are highlighted using orange arrows. In most interactomes, several preys associate to a given bait and might contact it directly or indirectly through intermediary proteins. **c**, Evolution over the course of TCR stimulation of the number of high-confidence bait–prey interactions, a value termed $N_{int}(t)$ with 't' corresponding to the time of stimulation. The proportion of these already reported in public databases is shown in orange. **d**, In the dot plot (left), the $N_{int}(t)$ values corresponding to each bait have been row-normalized to the maximum value it reached over the course of stimulation (see key). Also shown (right) using a $\log_{10}$ scale is the number of high-confidence bait–prey interactions corresponding to each bait, and the proportion of these that has been reported already. **e**, Annotation terms from Uniprot-Keywords and Uniprot-Protein families enriched in at least one of the 15 interactomes.

TCR-signaling network, we developed a CRISPR/Cas9-based pipeline that requires no mouse breeding and permits us to analyze in 4 months and, at organismal levels, the immune phenotype of mice deprived of select interacting proteins.

Results

Mapping the TCR signal-transduction network of primary T cells. To make the TCR signal-transduction network of primary T cells amenable to quantitative AP–MS analysis, we developed 15 lines of gene-targeted mice, each containing a canonical protein of the TCR-signaling network tagged at its amino (N) or carboxy (C) terminus with an affinity Twin-Strep-tag (OST) (Fig. 1a). Mice expressing the OST-tagged version of the cytosolic adaptors SLP-76 (LCP2) and GRB2, of the guanine nucleotide exchange factor VAV1 and of the evolutionarily related E3 ubiquitin-protein ligases CBL and CBLB have been described[4,7–9]. Here, we introduced ten additional OST-tagged mouse lines corresponding to the phosphatidylinositol 3,4,5-trisphosphate 5-phosphatase 1 SHIP1 (INPP5D), the PTKs LCK and ITK, the phospholipase PLC-γ1, the cytosolic adaptors NCK1, THEMIS and FYB (ADAP), the PTPases SHP1 (PTPN6) and PTPN22, and the NFATc2 transcription factor (Supplementary Fig. 1a and Methods). Analysis of mice homozygous for each of the OST-tagged alleles showed that their T cells developed properly (Supplementary Fig. 1b), yielding normal numbers of mature CD4+ and CD8+ T cells (Supplementary Fig. 1c) that had no defect in proliferation (Supplementary Fig. 1d), cytokine production (Supplementary Fig. 1e) and tyrosine phosphorylation (Supplementary Fig. 2) in response to TCR stimulation. T cells expressed the bait proteins at physiological levels (Supplementary Fig. 3a), and, after lysing them with the nonionic detergent *n*-dodecyl-β-D-maltoside, bait proteins were efficiently purified using Sepharose beads coupled to Strep–Tactin (Supplementary Fig. 3b,c), obviating potential variations resulting from the use of antibody specific for each bait.

Purified primary CD4+ T cells were briefly expanded in vitro to reach the substantial cell numbers required for AP–MS (see Methods). Our results thus reflect the composition of the TCR-signaling network of antigen-experienced conventional CD4+ T cells. To capture signaling dynamics, we defined, by AP–MS, the preys assembling around each bait before or after stimulation through cross-linkage of the TCR and CD4 for 30, 120, 300 and 600 s (Fig. 1a). For each time point, three independent biological replicates were performed and each biological replicate was analyzed in duplicate or triplicate by MS (technical replicates). To distinguish truly interacting proteins from nonspecific contaminants, we compared our data with control AP–MS experiments involving wild-type CD4+ T cells (Supplementary Fig. 4a,b). Data corresponding to 449 affinity purifications and 933 MS runs were analyzed using the MaxQuant software, and high-confidence interactors identified using a data-driven, false discovery rate (FDR)-controlled approach (ref. [6] and Methods). FDR values were used to evaluate the statistical significance of the enrichment observed at a given time point for a considered bait–protein interaction between CD4+ T cells isolated from OST-tagged and wild-type (control) mice (Supplementary Fig. 4c–e). High-confidence bait–prey interactions were defined as having FDR ≤ 3% for two consecutive time points of stimulation. We also measured the stoichiometry of bait–prey interactions using intensity-based absolute quantification (iBAQ)[10], and determined their changes after TCR engagement. The composition, stoichiometry and dynamics of the 15 interactomes are summarized in Supplementary Dataset 1.

Global analysis of the TCR signal-transduction network. Analysis of the interactomes assembling around each of the 15 baits revealed a bait–prey network composed of 277 unique proteins connected via 366 high-confidence interactions (Fig. 1b). Among them, 162 interactions have already been reported in human and mouse PPI databases that compile several cell types (Fig. 1c). As expected for a ligand-inducible signal-transduction PPI network, most of the 15 interactomes reached their highest complexity after TCR triggering (Fig. 1d). Such complexity peaked between 30 and 300 s in the case of the CBLB, GRB2, SLP-76, VAV1 and PLC-γ1 interactomes, and persisted up to 600 s of stimulation for the CBL and SHIP1 interactomes. Conversely, several of the preys found in the LCK and FYB interactomes were quickly released on TCR triggering.

The numbers of high-confidence bait–prey interactions varied widely across the analyzed baits, ranging from 1 (NCK1 bait) to 117 (LCK bait) (Fig. 1d). Only 20% of the identified preys were found in more than one interactome, suggesting that each of the selected baits exerts specific functions within the TCR-signaling network. In line with this, annotation enrichment analysis showed that several interactomes were enriched for unique biological processes, molecular functions, interacting protein domains and families (Fig. 1e). The annotations 'SH2 domain' and 'SH3 domain' were, however, shared by 9 and 10 of the 15 interactomes, respectively, reflecting the key role both domains play in shaping the TCR PPI network. Therefore, by identifying 366 high-confidence PPI within the proximal TCR signal-transduction network our approach revealed a complexity that was higher than expected.

Bait–prey interaction stoichiometries over the course of TCR stimulation. The median value of the distribution of the stoichiometries observed for all the documented bait–prey interactions increased following TCR activation (Fig. 2a), reflecting formation of protein

Fig. 2 | Evolution over 600 s of TCR stimulation of bait–prey interaction stoichiometry among the 15 interactomes. a, Distribution of the interaction stoichiometries of the 366 high-confidence bait–prey interactions observed for the 15 baits at each of the analyzed time points. Horizontal red lines correspond to median values and previously reported interactions are highlighted in orange. Note that $10^0 = 1$. **b**, Each dot plot corresponds to a given bait (denoted in red) and shows its interaction stoichiometry over the course of TCR stimulation with its 16 highest confidence preys (denoted in black and ranked according to their FDR value and maximum enrichment; see key for FDR color code). The total number of high-confidence interactions (*n*) established by a given bait is shown at the top of each dot plot (for instance $n = 87$ in the case of the CBL bait, and the full list of the 87 interactions can be found in the worksheet tab labeled 'CBL' of Supplementary Dataset 1). For a given bait–prey interaction, the interaction stoichiometry has been row-normalized to its maximum value observed over the course of TCR stimulation (Normal. stoichiometry). For instance, the FYB and LAT preys show a maximal binding to SLP-76 before and after 30 s of activation, respectively. Also shown on the right side of each dot plot is the maximal interaction stoichiometry (Maximum stoichiometry) reached by each of the documented bait–prey interactions over the course of TCR stimulation (dot size is commensurate with the value of the maximal interaction stoichiometry; see key). Orange and gray dots correspond to previously reported and undocumented interactors, respectively. In the case of a 'rich' interactome, as exemplified by the CBL interactome, all the 16 represented preys qualify as high-confidence preys, in that they all show FDR ≤ 3% at two consecutive time points of stimulation. In contrast, in the case of a 'sparse' interactome, as exemplified by the NCK1 interactome, a single prey (ARAP1) fulfills our stringent high-confidence criteria. The ACTBL2, PLBD1 and TMED10 preys interacted with NCK1 with an FDR ≤ 3% at a single condition of stimulation (t_{30s}), whereas preys such as WAS and TTN have FDR ≤ 6%. Such bait–prey interactions of lower confidence are listed in the tab 'bait–prey interactions' of Supplementary Dataset 1. Note that an FDR of 100% means that the prey does not interact with the bait at the considered time point.

assemblages of increasing complexity. The maximal interaction stoichiometries reached by the 366 documented bait–prey interactions over the course of TCR stimulation covered five orders of magnitude, ranging from 10^{-5} to 1.6, with a median value close to 10^{-3}. Among the PPIs described in the present study, those not reported in public databases showed a bias toward lower stoichiometry (Fig. 2a), highlighting the increased analytical depth afforded by the sensitivity of AP–MS compared with conventional biochemical approaches. Therefore, low-stoichiometry PPIs play a central role in the organization of the TCR-signaling

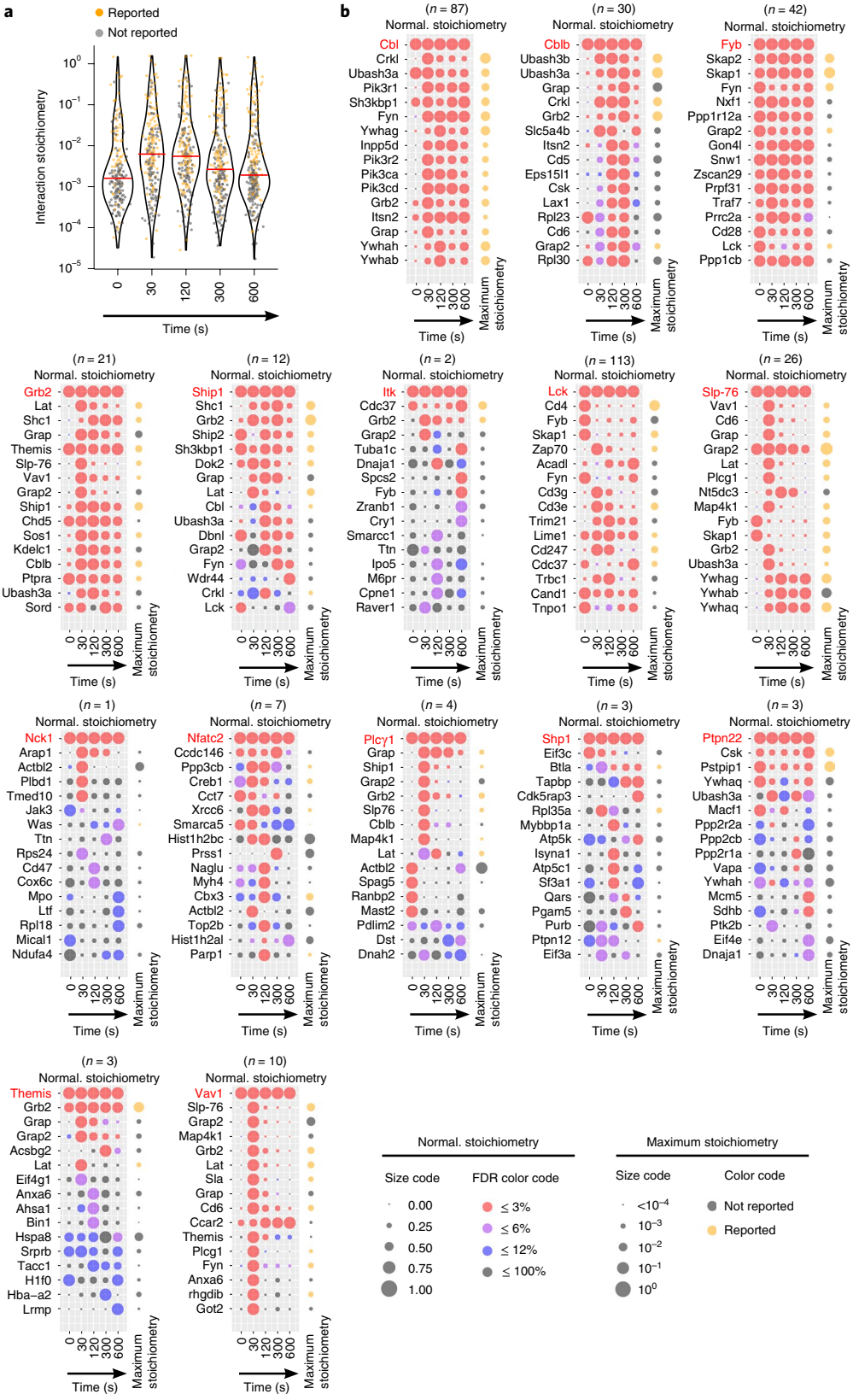

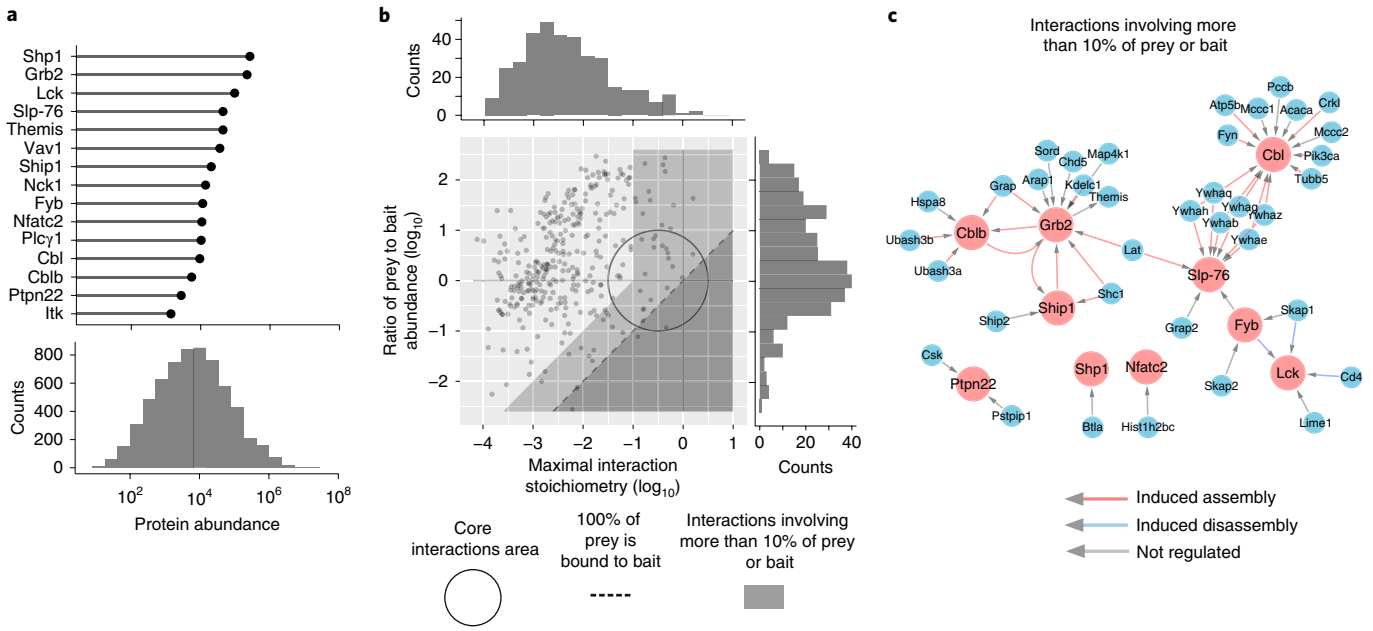

Fig. 3 | Organizing the 15 interactomes using cellular protein abundance and interaction stoichiometry. a, Cellular abundance distribution of the protein baits used for AP–MS (upper panel) and of the 6,343 proteins that were quantified in CD4+ T cells used for AP–MS (lower panel). Cellular abundances are shown as mean protein copy number per CD4+ T cell. **b**, Stoichiometry plot permits organization of each interactome. For each documented bait–prey interaction the ratio of bait to prey cellular abundance ('abundance stoichiometry' in $\log_{10}$ scale) was plotted as a function of the maximal interaction stoichiometry reached by the considered bait–prey interaction over the course of TCR stimulation ('interaction stoichiometry' in $\log_{10}$ scale)[6]. The stoichiometry plot represented in this panel corresponds to an overlay of the stoichiometry plots generated for each of the 15 baits (see Fig. 4). Each dot corresponds to one high-confidence bait–prey interaction. The circle (center: −0.5, radius: 1 in $\log_{10}$ scale) delimits the 'core interactions area' (see Results). The limit imposed on interaction stoichiometries by the relative bait–prey cellular abundance is shown by a dashed diagonal line that delimits a 'forbidden' area (dark gray). Dots lying on the dashed diagonal correspond to preys where 100% of them are bound to the corresponding bait in at least one of the stimulation conditions. The area including PPIs involving more than 10% of the prey, or of the bait, is also indicated (light gray). The distribution of the maximal bait–prey interaction stoichiometry and of the ratios of the prey to bait abundance are shown in the top and right margins, respectively. **c**, Bait–prey interactions involving more than 10% of the prey or of the bait. Baits and preys are denoted in red and blue, respectively. Arrows are color coded to specify whether the interaction is positively or negatively regulated by TCR stimulation, or not regulated.

network, making them prone to disruption in experiments relying on bait overexpression.

Dot plots were used to depict the normalized interaction stoichiometry of each bait with its 16 most-enriched preys over the course of TCR stimulation (Fig. 2b). The maximum interaction stoichiometry value reached over the course of stimulation was also shown. Note that interaction stoichiometry values can be stoichiometric (the bait and the prey interact with a 1:1 ratio), superstoichiometric (the bait and the prey interact with a greater than stoichiometric ratio) or substoichiometric (only a fraction of the bait interacts with a given prey). For instance, a bait such as VAV1 established transient and substoichiometric interactions with most of its preys. In contrast, SLP-76 interacted with GRAP2 (GADS) in a superstoichiometric and constitutive manner, whereas SLP-76 interactions with LAT, VAV1 and PLC-γ1 were transient and substoichiometric (Fig. 2b).

Integrating cellular protein abundances and interaction stoichiometries. CD4+ T cells isolated from the 15 OST-tagged mice and from wild-type mice were briefly expanded, as for AP–MS analysis, and the copy numbers per T cell (cellular protein abundance) of the distinct proteins they expressed were determined using whole-cell proteome analysis[11]. We were able to quantify 6,343 proteins that corresponded to 92% of the high-confidence preys identified here (Supplementary Dataset 2). The cellular abundances of the proteins used as baits were spread over two orders of magnitude, ranging from 1.3×10^3 for ITK to 2.6×10^5 for SHP1 (Fig. 3a). Consistent with immunoblot analysis (Supplementary Fig. 3a), the OST-tagged proteins showed cellular abundances comparable to those of their wild-type counterparts (Supplementary Fig. 5).

By combining cellular protein abundances and interaction stoichiometries, each of the 15 signalosomes was organized into a 'stoichiometry plot'[6]. Accordingly, for each documented bait–prey interaction the ratio of the bait to prey cellular abundance was plotted as a function of the maximal interaction stoichiometry reached by the considered bait–prey interaction over the course of TCR stimulation (Fig. 3b). This showed that a few (7%) of the identified high-confidence bait–prey interactions fell within a confined zone that is denoted as the 'core interactions area' and encompasses most of the permanent mammalian protein complexes collated in the CORUM database[12] (Fig. 3b). Among these are the FYB–SKAP1 (ref. [13]) and the SLP-76–GRAP2 (ref. [14]) permanent complexes, as well as TCR-inducible complexes that remained stable for several minutes after TCR stimulation as illustrated by phosphoserine-based complexes involving SLP-76 and three members of the 14-3-3 protein family (YWHAG, YWHAB and YWHAQ), and a complex involving CBLB and the PTPases UBASH3A and UBASH3B (Fig. 3c).

A region corresponding to bait–prey interactions involving at least 10% of the bait or prey expressed in a given T cell is also highlighted (Fig. 3b,c; light gray). The functional relevance of such interactions can be illustrated by the interaction observed between SHIP1 and its close relative SHIP2 (INPPL1) (Fig. 4), a PPI previously reported in platelets[15]. By catalyzing the hydrolysis of the phosphatidylinositol 3-kinase (PI3K) product, PtdIns(3,4,5)P_3, into PtdIns(3,4)P_2, SHIP1 and SHIP2 regulate effectors containing PtdIns(3,4,5)P_3- or PtdIns(3,4)P_2-selective pleckstrin homology

(PH) domains. Up to 1.3% of SHIP1 molecules were found associated with SHIP2 (Fig. 4), and such low interaction stoichiometry can be viewed as functionally inconsequential. However, considering that SHIP2 is 31-fold less abundant than SHIP1 in CD4+ T cells, 41% of the SHIP2 molecules available in a CD4+ T cell are thus associated with SHIP1 (Fig. 4). Accordingly, a SHIP1 deficiency will not only ablate a key enzymatic activity, but also free approximately half of the SHIP2 molecules present in CD4+ T cells from their interaction with SHIP1, allowing them to engage in rival interactions that might be beneficial or detrimental. Therefore, the possibility of integrating interaction stoichiometries and cellular abundances permits us to anticipate whether genetic or pharmacological perturbation of a single PPI can result in global network rewiring.

Accounting for the distinct function of the CBL and CBLB E3 ubiquitin-protein ligases. Our quantitative approach also permitted a high-resolution comparison of the signalosomes that form around CBL and CBLB (Fig. 4). Both comprised a receptor expressed at the plasma membrane (CD5), molecules involved in endocytosis (ITSN2, EPS15L1), adaptors (GRB2, GRAP, CRKL) and proteins (UBASH3A and the PTK CSK) that concur to the negative regulatory role of CBL and CBLB. Consistent with the distinct phenotypes of T cells deprived of CBL or CBLB, only CBL associated with FYN, six 14-3-3 protein family members, SH3KBP1, SHIP1 and several catalytic and regulatory subunits of PI3K. The co-recruitment of PI3K and SHIP1 by CBL likely sets in action proteins containing PH domains selective for PtdIns(3,4)P_2 (refs. [16,17]). Conversely, CBLB was the sole protein capable of sustained interaction with the UBASH3B PTPase. Importantly, 120 s after TCR engagement, CBLB associated with 58% of the available UBASH3B molecules, suggesting that the CD5–CBLB–UBASH3B axis provides a major quantitative contribution to TCR signal termination through ZAP70 dephosphorylation[18].

Accurate ab initio prediction of the GRB2 signalosome. The stoichiometry of a few bait–prey interactions identified here have been previously reported (FYB–SKAP1 (ref. [13]), SLP-76–GRAP2 (ref. [14]) and THEMIS–GRB2 (ref. [19])). Although our AP–MS-based stoichiometric calculations agreed with those reported values (Fig. 4), we further challenged their accuracy by testing their predictive power. Considering that the GRB2 adaptor constitutes a high-confidence prey in 9 of the 15 analyzed interactomes, we attempted to predict, ab initio, the stoichiometry of a simulated GRB2 interactome in which the nine baits binding to GRB2 play the role of preys. By combining the experimentally determined interaction stoichiometry of the nine baits with the GRB2 prey with their corresponding cellular abundances, we calculated the stoichiometry of 'reciprocal' interactions in which GRB2 constituted the bait (Fig. 5a and Methods). The resulting GRB2 interactome showed interaction stoichiometries that were in good agreement with those of the actual GRB2 interactome over all time points (Fig. 5b). Similar analysis of all the high-confidence interactions involving protein pairs corresponding to the 15 baits further supported the accuracy of our measurements (Fig. 5c). Such accuracy allowed us to quantify the numbers of TCR-inducible complexes involved in TCR signal propagation and diversification.

Extensive TCR signal diversification occurs at the level of LAT. By combining interaction stoichiometries and cellular protein abundances, we enumerated the maximum number of copies of each high-confidence bait–prey interaction that forms per T cell over the course of TCR stimulation. Since TCR signals are initiated at the plasma membrane, we specifically focused on those high-confidence interactions that form at the inner face of the plasma membrane and constitute seeds for signal propagation (Fig. 6a). Consistent with the view that LAT serves as an early point of signal diversification downstream of the TCR[2,20], constitutive binary complexes made of GRAP2–SLP-76, GRB2–SHIP1 and GRB2–THEMIS docked onto LAT following TCR engagement and nucleated the assembly of SLP-76-, SHIP1- and THEMIS-based signalosomes (Fig. 6b). Such seeds reached maximal numbers of copies per T cell 30 s after TCR engagement, ranging from about a hundred (LAT–GRB2–THEMIS) to several hundred (LAT–GRAP2–SLP-76 and LAT–GRB2–SHIP1) (Fig. 6b).

The signalosome assembling around the LAT–GRAP2–SLP-76 seed comprised PLC-γ1, the serine–threonine protein kinase MAP4K1 (HPK1), the FYB–SKAP1 binary complex, UBASH3A, GRB2, GRAP, six members of the 14-3-3 protein family, NCK1 and VAV1 (Fig. 7). The SLP-76–NCK1 interaction was of low stoichiometry and led to recruitment of the ARAP1 RHO-GAP with high confidence, of the WASp actin nucleation-promoting factor (WAS; FDR value of 4.7% at t_{600s}), and of the beta-actin-like protein 2 (ACTBL2; FDR ≤ 3% at t_{30s}). VAV1 recruited the SRC-like adaptor protein 1 (SLAP-1), two RHO GDP-dissociation inhibitors (ARHGDIA and ARHGDIB; both with FDR ≤ 3% at t_{30s}) and the small GTPase RHOA (FDR ≤ 3% at t_{30s}) (Supplementary Dataset 1). Therefore, when probed by AP–MS under physiological conditions, the signalosome nucleating around the LAT–GRAP2–SLP-76 seed couples the TCR to the production of inositol trisphosphate and diacylglycerol and to F-actin dynamics, a finding consistent with recent imaging studies[21,22].

The signalosome that forms around the LAT–GRB2–THEMIS seed is thought to play a key role during T cell development, in part due to its association with SHP1 (refs. [23–25]). SHP1 was, however, lacking in the THEMIS interactome of mature CD4+ T cells (Fig. 7 and Supplementary Dataset 1). To confirm such an unanticipated finding, we analyzed whether THEMIS was present in the SHP1 interactome of mature CD4+ T cells. As expected, the B and T lymphocyte attenuator (BTLA[26,27]) was found among the SHP1 preys, but THEMIS was still absent (Fig. 7). Along the same lines, the GRB2 interactome of mature CD4+ T cells contained THEMIS but lacked SHP1 (Fig. 7), suggesting that THEMIS–GRB2–SHP1 ternary complexes primarily form in developing thymic T cells.

Consistent with the compound enzymatic and scaffolding role of SHIP1, the signalosome assembling around the LAT–GRB2–SHIP1 seed comprised several adaptors (GRB2, GRAP, SH3KBP1 (CIN85), SHC1 and DOK2), and associated with a lower interaction stoichiometry to molecules such as UBASH3A, DBNL

Fig. 4 | Stoichiometry plots of the 15 baits. For each bait, the 20 bait–prey interactions with the largest enrichment and FDR ≤ 6% for at least one condition of stimulation are shown, and each stoichiometry plot is 'zoomed' on the area that includes them. Baits are shown as yellow dots. Red and blue dots correspond to preys that show an increased or decreased binding to the bait following TCR engagement. Gray dots correspond to preys whose association with the bait were not regulated by TCR stimulation. The size of the dots is commensurate with the maximal protein enrichment observed in OST-tagged CD4+ T cell samples compared with wild-type control CD4+ T cell samples. For instance, the SLP-76 stoichiometry plot shows that GRAP2 is more abundant than SLP-76 and that it binds to SLP-76 in a constitutive and superstoichiometric manner. The six documented 14-3-3 family members (YWHAB, YWHAE, YWHAG, YWHAH, YWHAQ and YWHAZ) are more abundant than SLP-76 and interact with it in a TCR-induced manner and a stoichiometry in the range 1.5–0.2. Cytosolic effectors, such as VAV1 and PLC-γ1, are slightly less abundant than SLP-76, and interact with it in a TCR-induced manner and a stoichiometry in the 0.008 range. Preys for which it was not possible to determine the cellular abundance are shown at the bottom of each stoichiometry plot. See Fig. 3b for a definition of the specified stoichiometry plot areas.

(an adaptor protein that binds F-actin), FYN and SHIP2 (Fig. 7 and Supplementary Dataset 1). Therefore, our quantitative and qualitative analyses of the SLP-76-, SHIP1- and THEMIS-based signalosomes emphasizes the unique contribution of LAT to TCR signal diversification, the breadth of which should be even greater when taking in account that the guanine nucleotide exchange factors SOS1 and SOS2 are also recruited via GRB2 to phosphorylated LAT molecules[4].

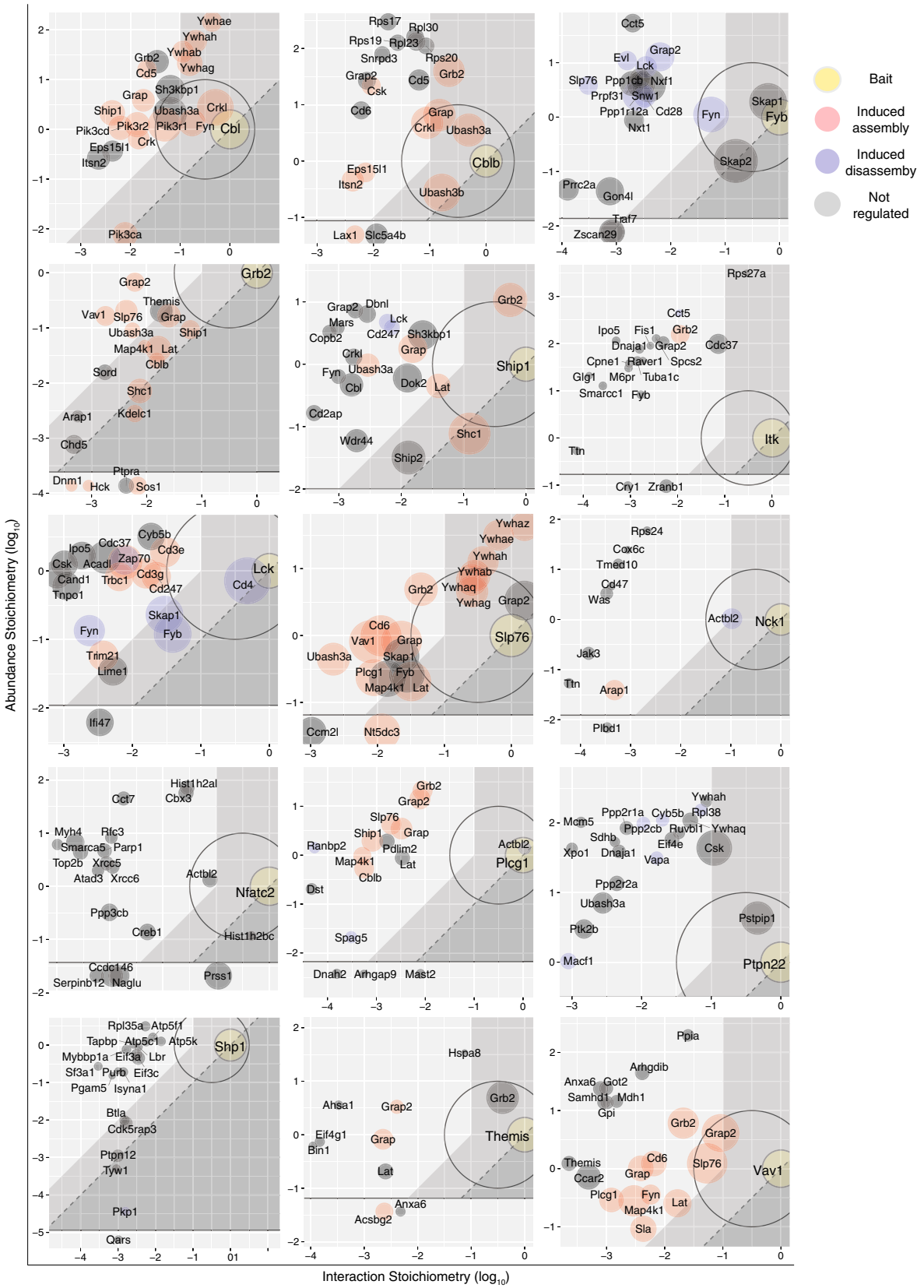

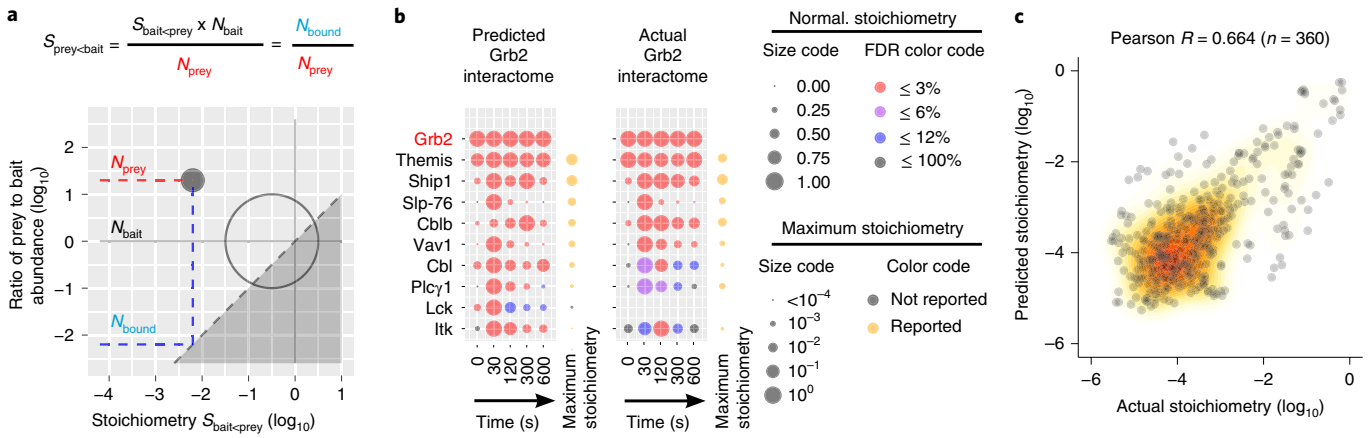

Fig. 5 | Ab initio prediction of the composition and stoichiometry of novel interactomes. a, By combining experimentally determined interaction stoichiometry between a bait A and a prey B ($S_{baitA<preyB}$) and their cellular abundance it is possible to calculate a 'reciprocal' stoichiometry in which B and A behave as the bait and the prey, respectively. **b**, Dot plots representing the interaction stoichiometries of the predicted GRB2 interactome (left, FDR ≤ 3%, ranked by maximum predicted stoichiometries) and of the experimentally determined GRB2 interactome (right, no FDR restriction). Note that the repertoire of preys of the predicted GRB2 interactome is confined to the repertoire of OST-tag baits capable of binding to GRB2. See key in Fig. 2b legend. **c**, Global comparison of experimentally determined and of predicted interaction stoichiometries corresponding to the 15 baits show a correlation coefficient of 0.66 and a median ratio of measured against predicted interaction stoichiometries of 3.7.

CD5, CD6 and LAX1 contribute to TCR signal diversification at the plasma membrane. Akin to LAT, several receptors and adaptors embedded in the T cell plasma membrane contain tyrosine residues that are capable of recruiting intracytoplasmic proteins following TCR-induced phosphorylation. Congruent with that view, CD6 was found in the SLP-76 and VAV interactomes, whereas CD5 was present in the CBL and CBLB interactomes (Fig. 7). The LAX1 transmembrane adaptor and CD6 were also found in the CBLB interactome, however with lower stoichiometries than CD5. The role of CD6 in T cell activation continues to be debated, whereas CD5 and LAX1 negatively regulate TCR signaling. The numbers of copies per T cell of CD5–CBL (198), CD5–CBLB (329), CD6–SLP-76 (484) and CD6–VAV1 (214) complexes induced on TCR activation were commensurate with those of LAT–SLP-76, LAT–SHIP1 and LAT–THEMIS complexes, unveiling their important quantitative contribution to TCR signal diversification. Moreover, the hundreds of copies of CBL- and CBLB-based signalosomes assembling around CD5 after 120 s of stimulation strengthened the view that CD5 constitutes a major mediator of TCR-induced ubiquitylation[9].

Assessment of the function of novel interacting proteins at organismal levels. Genomic editing by CRISPR/Cas9-based approaches permits the study of gene function in ex vivo primary T cells[28]. However, the role of genes involved in organismal function—such as lymphoid cell migration—cannot be assessed using ex vivo assays and requires development of mouse lines with homozygous loss-of-function mutations. To bypass such a fastidious approach, we used CRISPR/Cas9 to establish F_0 mice with biallelic deletions of a critical exon of genes coding for five poorly characterized preys identified in our interactomics dataset (see Methods). For each of the five tested genes (*AI467606*, *Arap1*, *Arhgap45*, *Cep85l* and *Nap1l4*), three single-guide RNAs were coinjected into zygotes and tail DNA from the five resulting F_0 mouse cohorts were genotyped by PCR. Of the resulting F_0 mice, 74% showed the expected biallelic DNA deletions and their blood was subjected to quantitative multiparametric analysis of myeloid and lymphoid cells (Fig. 8a). For instance, biallelic inactivation of the *Arghap45* gene, which codes for a functionally uncharacterized RHO GTPase-activating protein[29] found in the LCK interactome (Supplementary Dataset 1), produced the strongest phenotype among the five analyzed genes. *Arghap45* inactivation resulted in a severe reduction in blood CD45$^+$ cell numbers (Fig. 8a). Consistent with the pattern of *Arghap45* expression (http://www.immgen.org/databrowser/index.html), lymphocytes found in the blood were primarily affected by *Arghap45* inactivation (Fig. 8b). Analysis of the progeny of F_0 mice with biallelic *Arghap45* gene inactivation showed that their thymus and spleen were normal in terms of composition and absolute numbers, suggesting that ARGHAP45 has no detectable role during T and B cell development (Fig. 8c). In contrast, their lymph nodes showed a reduction in T and B cell numbers similar to that of F_0 mice (Fig. 8c,d). Considering that ARGHAP45 regulates actin cytoskeleton and cell spreading in transfected HeLa cells[29], our data suggest that in the absence of ARGHAP45, T and B cells have a reduced ability to enter into lymph nodes via diapedesis. Therefore, our reverse genetics approach constitutes a decision support tool permitting identification, in 4 months and without mouse breeding, of preys where ablation results in T cell phenotypes of interest when analyzed at organismal levels.

Discussion

We assessed the dynamics of the signalosomes assembling around 15 canonical proteins used by the TCR signal-transduction network in primary CD4$^+$ T cells. The unique possibility of integrating interaction stoichiometries and cellular abundances over the course of TCR stimulation allowed us to obtain key parameters for systems-level understanding of TCR signal propagation and diversification. For instance, we enumerated the number of signaling complexes that are used per T cell to convey TCR signals, and determined whether a fraction of the documented interacting proteins is left free to engage in alternative signalosomes over the course of stimulation. We also demonstrated that TCR signals divide into multiple branches at the level of the plasma membrane, resulting in the formation of CD5-, CD6-, BTLA- and LAX1-based signalosomes that assemble with kinetics comparable to the canonical LAT signalosome, and that contribute to TCR signal diversification due to their unique composition in adaptor and effector molecules.

Our time-resolved analysis also illustrated the speed at which signalosomes assemble and disassemble following TCR triggering. For instance, full-blown LAT–SLP-76 signalosomes were already present 30 s after TCR triggering. A finding that is consistent with the view that TCR signals are transmitted in a rapid manner, resulting in phosphorylation of TCR proximal components in 4 s, and

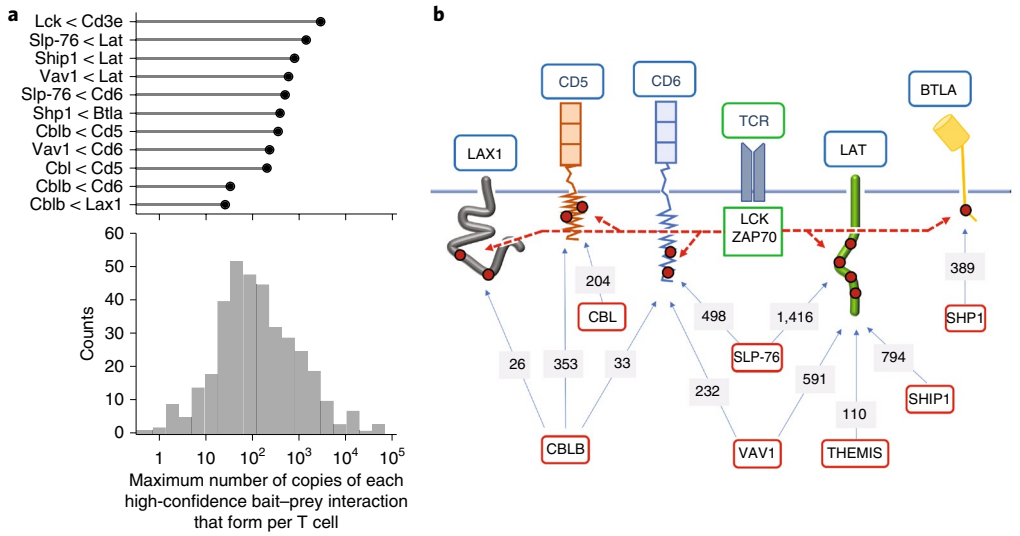

Fig. 6 | TCR signals branch at the level of the plasma membrane leading to the assembly of multiple signalosomes. a, For each of the 366 high-confidence bait–prey interactions, we calculated the maximum number of copies that form per CD4$^+$ T cell over 600 s of TCR stimulation and show their distribution in the lower panel. The distribution ranged from 0.4 to 7.0×10^4 copies per T cell with a median close to 1.1×10^2 copies per T cell. The high-confidence bait–prey interactions that involve a prey corresponding to a receptor (CD3ε, CD5, CD6, BTLA) or an adaptor (LAT, LAX1) associated with the T cell plasma membrane are shown in the upper panel. **b**, Following TCR engagement, signalosomes involving CBL, CBLB and VAV1 nucleate around the CD5 and CD6 transmembrane receptors in numbers comparable with those that form around the LAT adaptor via SLP-76, SHIP1 and THEMIS intermediates. Also shown are the BTLA coinhibitory receptor and the LAX1 adaptor that assemble signalosomes involving SHP1 and CBLB, respectively. Tyrosine residues (red dots) present in the intracytoplasmic segments of the depicted receptors and adaptors are phosphorylated by the LCK or ZAP70 PTK that associate with active TCR (dashed red arrows). Baits and preys are denoted using red and blue boxes, respectively. The maximum number (copies per T cell) of bait–prey complexes reached over the course of 600 s of TCR stimulation is specified over the arrows connecting the baits and the preys. For instance, the maximum number of CD5–CBLB complexes reached per T cell over 600 s of TCR stimulation is approximately 353.

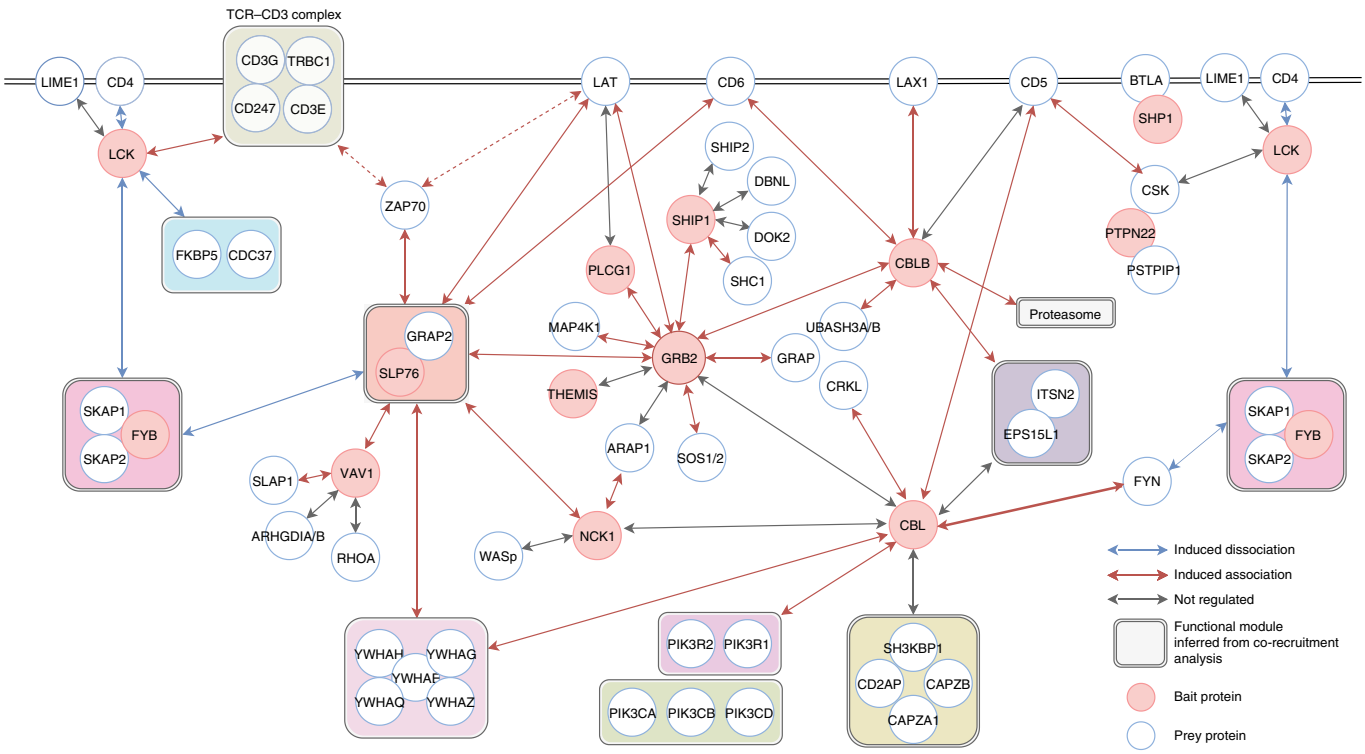

Fig. 7 | A model summarizing the protein–protein interactions occurring during the first 10 min of TCR activation. This diagram integrates data found in Figs. 2b and 4 and in Supplementary Datasets 1 and 2. It focuses on those high-confidence bait–prey interactions that (1) are regulated on TCR activation, (2) engage a large fraction of the bait or prey present in a given T cell or (3) are part of a functional module identified using co-recruitment analysis (Supplementary Fig. 6). For a deeper exploratory analysis, we included interactions with an FDR ≤ 3% for one consecutive condition of stimulation. The interactions specified by red dotted arrows have been established in a previous study[4].

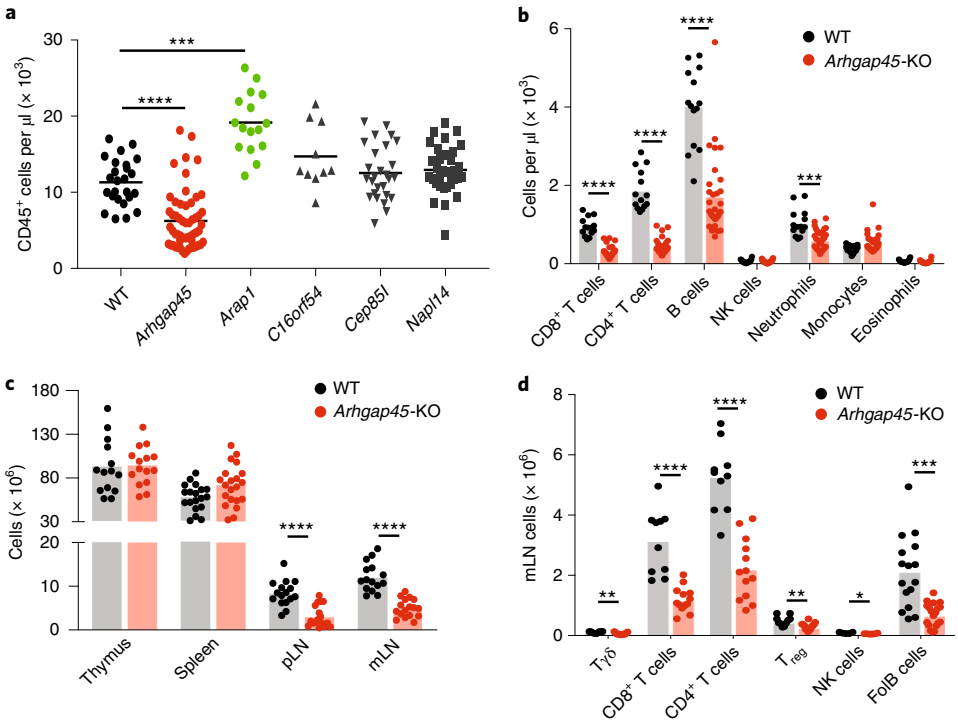

Fig. 8 | ARGHAP45 is crucial for proper T and B cell migration. a, Quantification of CD45$^+$ cells in the blood of wild-type mice and of F_0 mice with biallelic deletions of the *Arap1*, *AI467606*, *Arhgap45*, *Cep85l* and *Nap1l4* genes. Each symbol corresponds to a mouse and the mean (horizontal bar) is indicated. Among the analyzed *Arghap45* F_0 mice, six contain one *Arghap45* allele with a small deletion preserving its open reading frame and were used as internal control giving rise to normal blood phenotype. Wild type: $n=25$; *Arhgap45*: $n=56$; *Arap1*, $n=16$; *C16orf54*: $n=27$; *Cep85l*: $n=27$; *Nap1l4*: $n=33$. For each mutation, comparison was done relative to wild-type (WT) mice using unpaired Mann–Whitney U-test. ***$P=0.0002$; ****$P=0.000004$. In **a**–**d**, only significant values ($P<0.05$) are specified. **b**, Quantification of CD8$^+$ T cells, CD4$^+$ T cells, B cells, NK cells, neutrophils, monocytes and eosinophils in the blood of wild-type mice ($n=14$) and of F_0 mice with biallelic deletions in the *Arghap45* gene ($n=32$). ***$P=0.00021$; ****$P<0.00001$ (unpaired Holm–Sidak's multiple *t*-test corrected for multiple comparisons). **c**, Cellularity of the thymus, spleen, peripheral (pLN) and mesenteric (mLN) lymph nodes of the progeny of wild-type mice ($n=20$) and of F_0 mice with biallelic deletions in the *Arghap45* gene ($n=20$). ****$P<0.00001$ (unpaired Holm–Sidak's multiple *t*-test corrected for multiple comparisons). **d**, Quantification of γδ T cells (Tγδ), CD8$^+$ T cells, conventional CD4$^+$ T cells, regulatory CD4$^+$ T cells (T_{reg}), NK cells and follicular B (FolB) cells in the mesenteric lymph nodes of wild-type mice ($n=16$) and of F_0 mice with biallelic deletions in the *Arghap45* gene ($n=16$). *$P=0.017$; **$P=0.004$; ***$P=0.00003$; *****$P<0.00001$ (unpaired Holm–Sidak's multiple *t*-test corrected for multiple comparisons).

production of intracellular second messengers such as Ca^{2+} in 6–7 s (ref. [30]). Binding of MAP4K1 to SLP-76 peaked 30 s after TCR triggering. This led to serine–threonine phosphorylation of SLP-76 and GRAP2 (ref. [31]), and, as documented here, to the interaction of six 14-3-3 family members with SLP-76. These interactions were of high stoichiometry and correlated with dismantling of the LAT signalosome 120 s after TCR triggering, a finding that is consistent with the view that SLP-76 dissipates from TCR microclusters during their transport toward the center of the immunological synapse[32]. We showed that the CD5–CBL and CD5–CBLB signalosomes that formed following TCR engagement, in numbers comparable to the LAT signalosome, are primarily endowed with a negative regulatory role, likely contributing to the short temporal persistence of the LAT signalosome[33]. Smaller numbers of LAX1–CBLB complexes assembled, probably accounting for the milder negative regulation of TCR signals by LAX1.

Models accounting for the function of ITK, LCK, FYB and PTPN22 need to be revisited on the basis of the present quantitative interactomics study. On production of PtdIns(3,4,5)P_3, ITK is recruited to the plasma membrane through its PH domain and, after associating to the LAT–GRAP2–SLP-76 signalosome, it phosphorylates and activates PLC-γ1 (ref. [34]). We found that LCK was 70-fold more abundant than ITK in CD4$^+$ T cells, and that the LCK interactome was 60-fold larger than that of ITK. A reason for this last difference stems from the association of LCK with multiple transmembrane receptors and adaptors, among which we identified CD4, the TCR–CD3 complex, ZAP70, LAT, CD2, CD6, CD28, CD45 (PTPRC), the interleukin 2 receptor α and β subunits and LIME1. In contrast to ITK, which modulates the magnitude of calcium flux[34], LCK is responsible for initiating the entire TCR-signaling cascade and has T cell cancer-promoting activities. Accordingly, several of the molecules unique to the LCK interactome are likely to be devoted to controlling its high activity state and degradation. They corresponded to chaperones (CDC37, DNAJA1 and 2, FKBP5 and 8, HSP90AA1, HSP90AB1, ST13), several 26S proteasome subunits and CAND1, a member of the SCF E3 ubiquitin ligase complex. Moreover, the presence of RAB11B and of several GTP-binding proteins (IFI47, IRGM1, IFGGD) in the LCK interactome, likely fixes the activation threshold of naive T cells by controlling LCK subcellular localization[35]. The LCK interactome further differed from that of ITK by the presence of several proteins involved in nuclear export and import, suggesting unidentified roles for LCK.

FYB is rather unique among the analyzed baits in that it interacted with a large number of preys before TCR activation. Some of them, including FYB–SKAP1 and FYB–SKAP2, persisted after TCR activation, whereas others involving FYN, LCK and SLP-76 decreased on TCR activation. Analysis of the LCK and SLP-76 interactomes confirmed that the FYB–LCK and FYB–SLP-76 interactions diminished after TCR engagement, a finding that contrasted with results that suggest that FYB binds to SLP-76 in a TCR-inducible

manner[36]. Unexpectedly, FYB constitutively interacted with several proteins involved in pre-messenger RNA splicing (corresponding to the SNW1–PPIL1 complex, PRPF3 and PRRC2A), nuclear RNA export (corresponding to DDX3X3 and the NXF1 and NXT1 complexes) and mRNA stability (KHDRBS1–SAM68), a finding that is consistent with the presence of two nuclear localization sequences in FYB and its cytoplasmic and nuclear distribution[37]. Therefore, the composition and dynamics of the FYB interactome point to as-yet-unidentified roles of FYB in T cells.

Genetic variants of PTPN22 are among the strongest genetic risk factors for several human autoimmune diseases, the reasons for which remain unknown. We confirmed here that the constitutive interaction between PTPN22 and the adaptor proline–serine–threonine phosphatase-interacting protein 1 (PSTPIP1)[38]. Moreover, 7% of the PTPN22 molecules were associated to CSK before TCR stimulation. UBASH3A was found among the low-stoichiometry PTPN22 interactors, an observation that can be related to genome-wide association studies in which UBASH3A variants were linked to autoimmunity[39]. Moreover, after slightly relaxing the cutoff values (FDR ≤ 3% for one condition of stimulation), the structural A (PPP2R1A), regulatory B (PP2R2A) and catalytic C (PP2CB) subunits of the serine–threonine–protein phosphatase 2A (PP2A) were found constitutively associated to PTPN22. PP2A has recently been implicated in several autoimmune disorders[40], suggesting that PP2A contributes to the negative regulatory function of PTPN22 and its involvement in autoimmunity.

In conclusion, our study provides the most comprehensive analysis yet on the composition, stoichiometry and dynamics of the proximal TCR signal-transduction network in primary T cells. It illustrates the power of systems-level approaches to retrieve quantitative information on how TCR signals propagate and diversify at the level of the T cell plasma membrane for successful initiation and termination of T cell activation. Moreover, the possibility of integrating the cellular abundance of the interacting proteins and their interaction stoichiometry provides a quantitative and contextual picture of each documented PPI that supersedes the view resulting from conventional coimmunoprecipitation approaches. Importantly, it constitutes a framework that should help in rationalizing the phenotypic effect of genetic variations or drug treatments intended to block T cell activation, and in charting the redundant routes of signal propagation that a T cell might use to bypass a drug-targeted component, both of which constitute central issues in immune systems biology.

Online content

Any methods, additional references, Nature Research reporting summaries, source data, statements of code and data availability and associated accession codes are available at https://doi.org/10.1038/s41590-019-0489-8.

Received: 8 May 2019; Accepted: 5 August 2019;
Published online: 7 October 2019

References

1. Chakraborty, A. K. & Weiss, A. Insights into the initiation of TCR signaling. *Nat. Immunol.* **15**, 798–807 (2014).
2. Brownlie, R. J. & Zamoyska, R. T cell receptor signalling networks: branched, diversified and bounded. *Nat. Rev. Immunol.* **13**, 257–269 (2013).
3. Shah, N. H. et al. An electrostatic selection mechanism controls sequential kinase signaling downstream of the T cell receptor. *eLife* **5**, e20105 (2016).
4. Roncagalli, R. et al. Quantitative proteomics analysis of signalosome dynamics in primary T cells identifies the surface receptor CD6 as a Lat adaptor-independent TCR signaling hub. *Nat. Immunol.* **15**, 384–392 (2014).
5. Astoul, E., Edmunds, C., Cantrell, D. A. & Ward, S. G. PI 3-K and T-cell activation: limitations of T-leukemic cell lines as signaling models. *Trends Immunol.* **22**, 490–496 (2001).
6. Hein, M. Y. et al. A human interactome in three quantitative dimensions organized by stoichiometries and abundances. *Cell* **163**, 712–723 (2015).
7. Caron, E. et al. Precise temporal profiling of signaling complexes in primary cells using SWATH mass spectrometry. *Cell Rep.* **18**, 3219–3226 (2017).
8. Gaud, G. et al. The costimulatory molecule CD226 signals through VAV1 to amplify TCR signals and promote IL-17 production by $CD4^+$ T cells. *Sci. Signal.* **11**, eaar3083 (2018).
9. Voisinne, G. et al. Co-recruitment analysis of the CBL and CBLB signalosomes in primary T cells identifies CD5 as a key regulator of TCR-induced ubiquitylation. *Mol. Syst. Biol.* **12**, 876 (2016).
10. Schwanhausser, B. et al. Global quantification of mammalian gene expression control. *Nature* **473**, 337–342 (2011).
11. Wisniewski, J. R., Hein, M. Y., Cox, J. & Mann, M. A "proteomic ruler" for protein copy number and concentration estimation without spike-in standards. *Mol. Cell. Proteomics* **13**, 3497–3506 (2014).
12. Ruepp, A. et al. CORUM: the comprehensive resource of mammalian protein complexes—2009. *Nucleic Acids Res.* **38**, D497–D501 (2010).
13. Huang, Y. et al. Deficiency of ADAP/Fyb/SLAP-130 destabilizes SKAP55 in Jurkat T cells. *J. Biol. Chem.* **280**, 23576–23583 (2005).
14. Seet, B. T. et al. Efficient T-cell receptor signaling requires a high-affinity interaction between the Gads C-SH3 domain and the SLP-76 RxxK motif. *EMBO J.* **26**, 678–689 (2007).
15. Giuriato, S. et al. SH2-containing inositol 5-phosphatases 1 and 2 in blood platelets: their interactions and roles in the control of phosphatidylinositol 3,4,5-trisphosphate levels. *Biochem. J.* **376**, 199–207 (2003).
16. Liu, S. L. et al. Quantitative lipid imaging reveals a new signaling function of phosphatidylinositol-3,4-bisphophate: isoform- and site-specific activation of Akt. *Mol. Cell* **71**, 1092–1104.e5 (2018).
17. Goulden, B. D. et al. A high-avidity biosensor reveals plasma membrane PI(3,4)P2 is predominantly a class I PI3K signaling product. *J. Cell. Biol.* **218**, 1066–1079 (2018).
18. Yang, M. et al. K33-linked polyubiquitination of Zap70 by Nrdp1 controls CD8 T cell activation. *Nat. Immunol.* **16**, 1253–1262 (2015).
19. Paster, W. et al. GRB2-mediated recruitment of THEMIS to LAT is essential for thymocyte development. *J. Immunol.* **190**, 3749–3756 (2013).
20. Balagopalan, L., Kortum, R. L., Coussens, N. P., Barr, V. A. & Samelson, L. E. The linker for activation of T cells (LAT) signaling hub: from signaling complexes to microclusters. *J. Biol. Chem.* **290**, 26422–26429 (2015).
21. Kumari, S. et al. Actin foci facilitate activation of the phospholipase C-gamma in primary T lymphocytes via the WASP pathway. *eLife* **4**, e04953 (2015).
22. Ditlev, J. A. et al. A composition-dependent molecular clutch between T cell signaling condensates and actin. *eLife* **8**, e42695 (2019).
23. Choi, S. et al. THEMIS enhances TCR signaling and enables positive selection by selective inhibition of the phosphatase SHP-1. *Nat. Immunol.* **18**, 433–441 (2017).
24. Mehta, M. et al. Themis-associated phosphatase activity controls signaling in T cell development. *Proc. Natl Acad. Sci. USA* **115**, E11331–E11340 (2018).
25. Zvezdova, E. et al. Themis1 enhances T cell receptor signaling during thymocyte development by promoting Vav1 activity and Grb2 stability. *Sci. Signal.* **9**, ra51 (2016).
26. Murphy, T. L. & Murphy, K. M. Slow down and survive: enigmatic immunoregulation by BTLA and HVEM. *Annu. Rev. Immunol.* **28**, 389–411 (2010).
27. Celis-Gutierrez, J. et al. Quantitative interactomics in primary T cells provides a rationale for concomitant PD-1 and BTLA coinhibitor blockade in cancer immunotherapy. *Cell Rep.* **27**, 3315–3330.e7 (2019).
28. Seki, A. & Rutz, S. Optimized RNP transfection for highly efficient CRISPR/Cas9-mediated gene knockout in primary T cells. *J. Exp. Med.* **215**, 985–997 (2018).
29. de Kreuk, B. J. et al. The human minor histocompatibility antigen 1 is a RhoGAP. *PLoS ONE* **8**, e73962 (2013).
30. Huse, M. et al. Spatial and temporal dynamics of T cell receptor signaling with a photoactivatable agonist. *Immunity* **27**, 76–88 (2007).
31. Lasserre, R. et al. Release of serine/threonine-phosphorylated adaptors from signaling microclusters down-regulates T cell activation. *J. Cell. Biol.* **195**, 839–853 (2011).
32. Hashimoto-Tane, A. & Saito, T. Dynamic regulation of TCR-microclusters and the microsynapse for T cell activation. *Front. Immunol.* **7**, 255 (2016).
33. Yi, J., Balagopalan, L., Nguyen, T., McIntire, K. M. & Samelson, L. E. TCR microclusters form spatially segregated domains and sequentially assemble in calcium-dependent kinetic steps. *Nat. Commun.* **10**, 277 (2019).
34. Andreotti, A. H., Joseph, R. E., Conley, J. M., Iwasa, J. & Berg, L. J. Multidomain control over TEC kinase activation state tunes the T cell response. *Annu. Rev. Immunol.* **36**, 549–578 (2018).
35. Bouchet, J. et al. Rab11-FIP3 regulation of lck endosomal traffic controls TCR signal transduction. *J. Immunol.* **198**, 2967–2978 (2017).
36. Geng, L., Raab, M. & Rudd, C. E. Cutting edge: SLP-76 cooperativity with FYB/FYN-T in the up-regulation of TCR-driven IL-2 transcription requires SLP-76 binding to FYB at Tyr595 and Tyr651. *J. Immunol.* **163**, 5753–5757 (1999).

37. Veale, M. et al. Novel isoform of lymphoid adaptor FYN-T-binding protein (FYB-130) interacts with SLP-76 and up-regulates interleukin 2 production. *J. Biol. Chem.* **274**, 28427–28435 (1999).
38. Marcos, T. et al. Proline-serine-threonine phosphatase interacting protein 1 inhibition of T-cell receptor signaling depends on its SH3 domain. *FEBS J.* **281**, 3844–3854 (2014).
39. Stanford, S. M., Mustelin, T. M. & Bottini, N. Lymphoid tyrosine phosphatase and autoimmunity: human genetics rediscovers tyrosine phosphatases. *Semin. Immunopathol.* **32**, 127–136 (2010).
40. Xu, Q. et al. Phosphatase PP2A is essential for TH17 differentiation. *Proc. Natl Acad. Sci. USA* **116**, 982–987 (2019).

Acknowledgements

We thank D. Mori, C. Wülfing (University of Bristol) and A. Zarubica for discussions and E. Bergot, S. Li, T. Chao, S. Durand and the late F. Danjan for technical help. This work was supported by CNRS, INSERM, the European Research Council (ERC) under FP7 program (grant agreement no. 322465 (INTEGRATE), to B.M.) and the European Union's Horizon 2020 research and innovation program (grant agreement no. 787300 (BASILIC), to B.M.), Agence Nationale de la Recherche (BASILIC project, to M.M.), the MSDAVENIR Fund (to B.M.), the Investissement d'Avenir program of the French Ministry of Research ProFI (Proteomics French Infrastructure, ANR-10-INBS-08, to O.B.-S.), and PHENOMIN (French National Infrastructure for mouse Phenogenomics; ANR-10-INBS-07, to B.M.), the National Natural Science Foundation of China (grant nos 81471595 and 31400759, to Y.L.) and the Education Department of Henan Province, China (16HASTIT030, to Y.L.) and by fellowships from the INTEGRATE (to M.G.M, G.V., K.K. and K.C.), MSDAVENIR (to Y.O.) and PHENOMIN (to L.G.) projects.

Author contributions

B.M., R.R. and G.V. conceived the project. B.M. and F.F supervised the construction of OST-tagged mice. R.R. and M.M. performed the experiments shown in Supplementary Figs. 1–3 with the help of L.G., Y.O. and M.G.M. K.K. characterized the SHIP1^{OST}, PLC-γ1^{OST} and PTPN6^{OST} mice with the help of J.C. A.G.de P., K.C. and O.B.-S. performed the MS experiments. G.V. designed the computational and bioinformatics analysis. Y.L., M.M., H.L. and B.M designed the experiments shown in Fig. 8 and L.L., L.Z. and H.W. performed them. B.M., G.V. and R.R. wrote the manuscript.

Competing interests

The authors declare no competing interests.

Additional information

Supplementary information is available for this paper at https://doi.org/10.1038/s41590-019-0489-8.

Correspondence and requests for materials should be addressed to Y.L., R.R. or B.M.

Peer review information Laurie A. Dempsey was the primary editor on this article and managed its editorial process and peer review in collaboration with the rest of the editorial team.

Reprints and permissions information is available at www.nature.com/reprints.

Publisher's note Springer Nature remains neutral with regard to jurisdictional claims in published maps and institutional affiliations.

Methods

Mice. Mice were on C57BL/6 background, sex matched and 9 weeks old. They were maintained in specific pathogen-free conditions and used in accordance with institutional committee and European (Marseille) and Chinese (Xinxiang) guidelines for animal care. CBL^{OST} mice (B6-*Cbl*^{tm1Mal}), CBLB^{OST} mice (B6-*Cblb*^{tm1Ciphe}), GRB2^{OST} mice (B6-*Grb2*^{tm1Mal}), SLP-76^{OST} (B6-*Lcp2*^{tm2Mal}) and VAV1^{OST} mice (B6-*Vav1*^{tm1Mal}) have been described[4,7–9]. Generation of FYB^{OST} (B6-*Fyb*^{tm1Ciphe}), SHIP1^{OST} (B6-*Inpp5d*^{tm1Mal}), ITK^{OST} (B6-*Itk*^{tm1Ciphe}), LCK^{OST} (B6-*Lck*^{tm4Mal}), NCK1^{OST} (B6-*Nck1*^{tm1Mal}), NFATC2^{OST} (B6-*Nfatc2*^{tm1Ciphe}), PLC-γ1^{OST} (B6-*Plcg1*^{tm1Ciphe}), SHP1^{OST} (B6-*Ptpn6*^{tm1Mal}), PTPN22^{OST} (B6-*Ptpn22*^{tm2Ciphe}) and THEMIS^{OST} (B6-*Themis*^{tm1Ciphe}) mice is described in Supplementary Note 1. Identification of OST-targeted alleles was performed by PCR using the pair of primers specified in Supplementary Table 1. Generation of F_0 mice with biallelic null mutations in the *Nap1l4*, *Arhgap45*, *AI467606*, *Cep85l* and *Arap1* genes is described in Supplementary Note 2, and their analysis by flow cytometry is described in Supplementary Note 3.

Biochemical validation of OST-tagged mice. CD4$^+$ T cells from wild-type mice and from each of the OST-tagged mice reported here were lysed in buffer (50 mM Tris, pH 7.5, 135 mM NaCl, 0.5 mM EDTA, 10% glycerol, 0.2% *n*-dodecyl-β-D-maltoside) supplemented with protease and phosphatase inhibitors. After 10 min of incubation on ice, cell lysates were centrifuged at 21,000*g* for 5 min at 4 °C. Postnuclear lysates were used either as whole-cell lysates or immunopurified on Strep–Tactin (see section on 'Affinity purification of OST-tagged protein complexes'). Samples eluted from Strep–Tactin and whole-cell lysates were loaded on 8% SDS–PAGE gel and subsequently analyzed by immunoblot with specific antibodies: anti-ITK (sc-23902), anti-PTPN6 (sc-287), anti-SHIP1 (sc-8425) and anti-NFATc2 (sc-7296) were from Santa Cruz Biotechnology, anti-PLC-γ1 (2822), anti-VAV1 (2502), anti-SLP-76 (4958), anti-ZAP70 (2705) and anti-LCK (2752) were from Cell Signaling Technology, anti-THEMIS (PA5-19288) was from Thermo Scientific, anti-NCK1 (610100) was from BD Biosciences, anti-FYB (07-546) was from Millipore and anti-PTPN22 was a gift from Genentech. Addition of the OST sequence had no effect on the expression of most tagged protein polypeptides (Supplementary Fig. 3a), with the exception of SHP1-OST polypeptides that were twofold reduced compared with their wild-type counterparts (see Supplementary Note 4).

Flow cytometry analysis of T cells from OST-tagged mice. Stained cells were analyzed using an LSRII system (BD Biosciences) and Diva software (BD Biosciences). Cell viability was evaluated using SYTOX Blue (Life Technologies). The following antibodies were used: anti-CD5 (53-7.3), anti-CD4 (RM45) and anti-CD44 (Im7) from BD Biosciences, anti-CD8 (53-6.7), anti-CD25 (PC61), anti-TCRβ (H57-597), anti-TCRγδ (GL3) and anti-CD19 (6D5) from BioLegend.

Functional analysis of CD4$^+$ T cells from OST-tagged mice. For proliferation and IL-2 secretion assay, purified CD4$^+$ T cells were stimulated with plate-bound anti-CD3 (145-2C11; Exbio) and soluble anti-CD28 (37-51; Exbio). After 48 h of culture, T cell proliferation was assessed with CellTiter-Glo Luminescent (Promega). The resulting luminescence, which is proportional to the ATP content of the culture, was measured with a Victor 2 luminometer (Wallac, Perkin Elmer Life Science). IL-2 production was measured with a DuoSet ELISA test (R&D Systems).

CD4$^+$ T cell isolation and short-term expansion for AP–MS analysis. CD4$^+$ T cells were purified (>95%) from pooled lymph nodes and spleens with Dynabeads Untouched Mouse CD4$^+$ T Cell Kit (Life Technologies). Purified CD4$^+$ T cells were expanded for 48 h with plate-bound anti-CD3 (145-2C11; 5 μg ml^{-1}) and soluble anti-CD28 (37-51; 1 μg ml^{-1}), both from Exbio. After 48 h of culture, CD4$^+$ T cells were collected and grown in the presence of IL-2 (10 U ml^{-1}) for 48 h before AP–MS analysis.

Stimulation and lysis of CD4$^+$ T cells before AP–MS analysis. Short-term expanded CD4$^+$ T cells (100 × 10^6) from wild-type mice and OST-tagged mice were incubated with anti-CD3 (0.2 μg per 10^6 cells; 145-2C11, Exbio) and anti-CD4 (0.2 μg per 10^6 cells; GK1.5, Exbio) on ice for 15 min, followed by one round of washing at 4 °C. Cells were then incubated at 37 °C for 5 min and then stimulated at 37 °C with a purified rabbit anti-rat Ig (0.4 μg per 10^6 cells; Jackson ImmunoResearch) for 30, 120, 300 and 600 s, or left unstimulated. Stimulation was stopped by the addition of a twice-concentrated lysis buffer (100 mM Tris, pH 7.5, 270 mM NaCl, 1 mM EDTA, 20% glycerol, 0.4% *n*-dodecyl-β-D-maltoside) supplemented with protease and phosphatase inhibitors. After 10 min of incubation on ice, cell lysates were centrifuged at 21,000*g* for 5 min at 4 °C. Postnuclear lysates were then used for affinity purification.

Affinity purification of OST-tagged protein complexes. Equal amounts of postnuclear lysates from wild-type mice and OST-tagged mice were incubated with Strep–Tactin Sepharose beads (IBA) for 1.5 h at 4 °C on a rotary wheel. Beads were then washed five times with 1 ml of lysis buffer in the absence of detergent and of protease and phosphatase inhibitors. Proteins were eluted from the Strep–Tactin Sepharose beads with 2.5 mM D-biotin.

Tandem MS analysis. Following affinity purification, protein samples were partially air dried in a SpeedVac concentrator, reconstituted in Laemmli buffer containing dithiothreitol (25 mM) and heated at 95 °C for 5 min. Cysteines were alkylated for 30 min at room temperature by the addition of iodoacetamide (90 mM). Protein samples were loaded on an SDS–PAGE gel (0.15 × 3 × 8 cm^3) and subjected to electrophoresis. Migration was stopped as soon as the protein sample entered the gel. The gel was briefly stained with Coomassie blue, and a single slice containing the whole protein sample was excised. The gel slice was washed twice with 100 mM ammonium bicarbonate and once with 100 mM ammonium bicarbonate–acetonitrile (1:1). Proteins were digested in-gel overnight at 37 °C using 0.6 μg modified sequencing grade trypsin (Promega) in 50 mM ammonium bicarbonate. The resulting peptides were extracted from the gel by one round of incubation (15 min, 37 °C) in 50 mM ammonium bicarbonate and two rounds of incubation (15 min each, 37 °C) in 10% formic acid–acetonitrile (1:1). The three extracted fractions were pooled and air dried. Peptides were further purified on a C18 ZipTip (Millipore) and dried again. Tryptic peptides were resuspended in 20 μl of 2% acetonitrile and 0.05% trifluoroacetic acid and analyzed by MS. A mix of standard synthetic peptides (iRT Kit; Biognosys) was spiked in all samples to monitor the stability of the nano-liquid chromatography (LC)–MS system during the analytical sequence. Peptides were analyzed by nano-LC coupled to tandem MS, using an UltiMate 3000 system (NCS-3500RS Nano/Cap System; Dionex) coupled to an Orbitrap Velos Pro mass spectrometer (ThermoFisher Scientific). For each sample, 5 μl was loaded on a C18 precolumn (300 μm inner diameter × 5 mm; Dionex) in a solvent made of 2% acetonitrile and 0.05% trifluoroacetic acid, at a flow rate of 20 μl min^{-1}. After 5 min of desalting, the precolumn was switched online with the analytical C18 column (75 μm inner diameter × 50 cm, in-house packed with Reprosil C18) equilibrated in 95% solvent A (5% acetonitrile, 0.2% formic acid) and 5% solvent B (80% acetonitrile, 0.2% formic acid). Peptides were eluted using a 5–50% gradient of solvent B over 105 min and a flow rate of 300 nl min^{-1}. The LTQ Orbitrap Velos was operated in data-dependent acquisition mode with Xcalibur software. Survey scan MS was acquired in the Orbitrap in the 350–2,000 *m/z* range, with the resolution set to a value of 60,000. The survey scans of the 20 most intense ions were selected for fragmentation by collision-induced dissociation, and the resulting fragments were analyzed in the linear trap. Dynamic exclusion was used within 60 s to prevent repetitive selection of the same peptide. Technical LC–MS measurement replicates were performed for each sample (duplicate or triplicate runs depending on the series).

Protein identification and quantification for interaction proteomics. Raw MS files were processed with MaxQuant software (v.1.5.2.8) for database search with the Andromeda search engine and quantitative analysis. Data were searched against *Mus musculus* entries of the UniProtKB protein database (release UniProtKB/Swiss-Prot + TrEMBL 2017_01, 89,297 entries including isoforms), the Biognosys iRT peptides, the One-Strep-tag peptide sequence and the set of common contaminants provided by MaxQuant. Carbamidomethylation of cysteines was set as a fixed modification, whereas oxidation of methionine, protein N-terminal acetylation and phosphorylation of serine, threonine and tyrosine were set as variable modifications. Specificity of trypsin digestion was set for cleavage after K or R residues, and two missed trypsin cleavage sites were allowed. The precursor mass tolerance was set to 20 ppm for the first search and 4.5 ppm for the main Andromeda database search. The mass tolerance in tandem MS mode was set to 0.5 Da. Minimum peptide length was set to seven amino acids, and minimum number of unique or razor peptides was set to 1 for validation. The *I* = L option of MaxQuant was enabled to avoid erroneous assignation of undistinguishable peptides belonging to very homologous proteins. Andromeda results were validated by the target decoy approach using a reverse database, with a FDR value set at 1% at both peptide sequence match and protein level. For label-free relative quantification of the samples, the match between runs option of MaxQuant was enabled with a match time window of 1 min, to allow cross-assignment of MS features detected in the different runs, after alignment of the runs with a time window of 20 min. Protein quantification was based on unique and razor peptides. The minimum ratio count was set to 1 for label-free quantification calculation, and computation of the iBAQ metric was also enabled.

Statistics and data reproducibility. From the 'proteinGroups.txt' files generated by MaxQuant with the options described above, protein groups with negative identification scores were filtered, as well as proteins identified as contaminants. Because protein groups were mapped using a redundant database (combining TrEMBL and Swiss-Prot), some protein groups corresponded to the same gene name. In such situations, protein intensities in a given sample were summed over the redundant protein groups. Protein intensities were log transformed before being normalized across all conditions (condition of stimulation, biological and technical replicates) by the median intensity. Normalized intensities corresponding to different technical replicates were averaged and missing values were replaced after estimating background binding from wild-type intensities. For each bait and each condition of stimulation, we used a two-tailed Welch's *t*-test to compare normalized protein intensities detected in OST-tagged samples across all biological replicates with wild-type intensities pooled from all conditions of stimulation. Logarithmized fold change and corresponding *P* values were used to generate a

global volcano plot representing interactions from all baits and all conditions of stimulation (Supplementary Fig. 4c). Asymmetry of this global volcano plot was used to define regions corresponding to different FDR values[6]. Briefly, the volcano plot was divided into different regions by a line of equation $f(x) = c/(|x| - x_0)$. For a given set of parameters (c, x_0), the FDR is computed using the number of proteins falling in the upper left and right regions, denoted as n_{left} and n_{right} respectively, according to the formula:

$$\mathrm{FDR}(c, x_0) = n_{left} / (n_{left} + n_{right})$$

The FDR value of a given bait–prey interaction at a given stimulation time is then taken as the maximum FDR value calculated across all (c, x_0) parameters. Bait–prey interactions with an FDR value ≤3% for two consecutive stimulation times were identified and referred to as high-confidence interactions.

Calculation of interaction stoichiometries. For a given condition of stimulation (represented by the time of stimulation t, with $t = 0$ corresponding to the unstimulated condition), the stoichiometry of the interaction between a given bait and a prey x (denoted bait < x) was calculated using:

$$S_{\mathrm{bait}<x}(t) = \langle I_{\mathrm{OST},x}(t)\rangle / \langle I_{\mathrm{OST,bait}}(t)\rangle \times N_{\mathrm{pep,bait}} / N_{\mathrm{pep},x}$$

N_{pep} corresponds to the number of tryptic peptides theoretically observables and brackets represent averages across all biological replicates. We also computed stoichiometries independently for each biological replicate, denoted $S_{\mathrm{bait}<x}(t; \mathrm{rep})$, and those values were used to quantify correlation in recruitment between different preys (see section on 'Co-recruitment analysis').

High-resolution MS characterization of the CD4⁺ T cell proteome. For proteome analysis, CD4⁺ T cells from wild-type and from OST-tagged mice were briefly expanded in vitro as described for AP–MS experiments. Cell pellets (5×10^6 cells) were incubated with 150 µl of lysis buffer containing Tris 50 mM, pH 7.5, EDTA 0.5 mM, NaCl 135 mM, SDS 1% for 10 min on ice and subjected to sonication with a Bioruptor ultrasonicator. Protein concentration was determined using a detergent-compatible assay (DC assay, Bio-Rad) and total protein amounts were adjusted across samples. Each protein sample was migrated briefly on SDS–PAGE gel and processed for in-gel digestion as described for AP–MS. Resulting peptide mixtures were analyzed with a fast-sequencing QExactivePlus Orbitrap mass spectrometer (Thermo Scientific), using long gradient runs (5–50% gradient of solvent B over 240 min). Survey MS scans were acquired in the Orbitrap in the 350–2000 m/z range with a resolution of 70,000, the ten most intense ions per survey scan were selected for higher energy collisional dissociation fragmentation and the resulting fragments were analyzed at a resolution of 17,500 in the Orbitrap. Raw MS files were processed with MaxQuant as described in the section 'Protein identification and quantification for interaction proteomics', with a search against *Mus musculus* entries of the UniProtKB/Swiss-Prot protein database, using a tolerance of 20 ppm for MS/MS in the Orbitrap.

Calculation of cellular protein abundance. Analysis of the proteome of CD4⁺ T cells from 14 mice lines (corresponding to 1 wild-type and 13 distinct OST-tagged genetic backgrounds) identified 4,643 protein groups. Protein entries from the MaxQuant 'proteinGroups.txt' output were first filtered to eliminate entries from reverse and contaminant databases. Cellular protein abundances were determined from raw intensities using the protein ruler methodology[11], using the following relationship: protein copies per cell = (protein MS signal × N_A × DNA mass)/(M × histone MS signal), where N_A is Avogadro's constant, M is the molar mass of the protein and the DNA mass of a diploid mouse cell is estimated to be 5.5209 pg. Cellular protein abundances were log transformed and averaged sequentially over technical replicates, and biological replicates for all genetic backgrounds. Overall, the cellular protein abundance could be estimated for 4,148 protein groups and averaged across 14 different backgrounds.

Peptide fractionation was further used to increase the depth of the CD4⁺ T cell proteome before and after stimulation through the TCR and CD4. This led to the identification of 6,388 protein groups. Cellular protein abundances for 6,104 protein groups were determined as described and averaged across all conditions of stimulation. To merge our two proteomes, the median averaged cellular protein abundance of the second proteome was adjusted to that of the first proteome. A total of 6,343 unique majority protein identities (which contained at least half of a protein groups razor + unique peptides) were then identified across all protein groups (Supplementary Dataset 2). In the case where a majority protein identity was identified in both proteomes, the cellular protein abundance value was taken from the proteome where the highest number of razor + unique peptides was associated to this protein identity.

Calculation of reciprocal stoichiometries. For all bait A–prey B interactions A < B, the stoichiometry of the reciprocal interaction B < A was calculated using the following relationship:

$$S_{\mathrm{B}<\mathrm{A}} = S_{\mathrm{A}<\mathrm{B}} \times N_{\mathrm{A}} / N_{\mathrm{B}}$$

where N_A and N_B are cellular protein abundances of A and B, respectively. Note that reciprocal stoichiometries could only be computed when the cellular abundances of both proteins were available. Comparison between experimentally determined stoichiometries and stoichiometries predicted from the reciprocal interaction was performed in all cases where both A and B were protein baits and both A < B and B < A interaction stoichiometries were quantified.

Co-recruitment analysis. We previously demonstrated that the occurrence of temporal correlations in the recruitment of two preys to a given bait can be used to infer functional or physical relationships between these preys and to construct a co-recruitment network[9]. The rationale behind this reasoning is that physically interacting preys, or preys cooperating toward a peculiar function, should have similar profiles of recruitment to a given bait as a function of time of TCR stimulation. Here, we extended this approach to the analysis of recruitment correlations within the 15 interactomes. Within each interactome we quantified correlations in interaction stoichiometries for all pairs of high-confidence preys and selected strongly correlated pairs (Pearson $R \geq 0.8$ with an associated $P \leq 0.05$). To limit the maximum degree of the resulting correlation network, we only kept the two preys that were the most strongly correlated with a given prey. Correlation networks from individual interactomes were then merged to form a single global co-recruitment network, the finer structure of which was divided into protein communities using a modularity optimization algorithm[41].

Comparison with PPIs reported in databases. Bait–prey interactions identified in this study were compared to PPIs previously reported between human or mouse proteins in the publicly available BioGrid (https://thebiogrid.org), IntAct (https://www.ebi.ac.uk/intact/), MINT (https://mint.bio.uniroma2.it) and HPRD (http://www.hprd.org/) databases.

Annotation enrichment analysis. We annotated the different identified proteins using Uniprot-Protein families and Uniprot-Keywords. We used a hypergeometric test to determine whether an annotation term was statistically enriched in a given interactome compared with a background composed of all proteins identified in this interactome (without any filtering based on the FDR). Annotations that were represented by at least two high-confidence preys (FDR ≤ 3% for two consecutive stimulation times) and had an enrichment greater than twofold with a P value lower than 0.05 were selected as enriched terms. We used the same procedure to analyze annotation enrichment within functional communities identified in the co-recruitment network, with the background corresponding to the set of high-confidence preys.

Reporting Summary. Further information on research design is available in the Nature Research Reporting Summary linked to this article.

Data availability

The data that support the findings of this study are available from the corresponding authors upon request. The mass spectrometry proteomics data have been deposited to the ProteomeXchange Consortium via the PRIDE partner repository (http://www.ebi.ac.uk/pride) with the dataset identifiers PXD012826, PXD007660 and PXD003972.

References

41. Clauset, A., Newman, M. E. & Moore, C. Finding community structure in very large networks. *Phys. Rev. E* **70**, 066111 (2004).

nature research

Corresponding author(s): Bernard Malissen

Last updated by author(s): 2019/30/07

Reporting Summary

Nature Research wishes to improve the reproducibility of the work that we publish. This form provides structure for consistency and transparency in reporting. For further information on Nature Research policies, see Authors & Referees and the Editorial Policy Checklist.

Statistics

For all statistical analyses, confirm that the following items are present in the figure legend, table legend, main text, or Methods section.

n/a	Confirmed	
☐	☒	The exact sample size (*n*) for each experimental group/condition, given as a discrete number and unit of measurement
☐	☒	A statement on whether measurements were taken from distinct samples or whether the same sample was measured repeatedly
☐	☒	The statistical test(s) used AND whether they are one- or two-sided *Only common tests should be described solely by name; describe more complex techniques in the Methods section.*
☐	☒	A description of all covariates tested
☐	☒	A description of any assumptions or corrections, such as tests of normality and adjustment for multiple comparisons
☐	☒	A full description of the statistical parameters including central tendency (e.g. means) or other basic estimates (e.g. regression coefficient) AND variation (e.g. standard deviation) or associated estimates of uncertainty (e.g. confidence intervals)
☐	☒	For null hypothesis testing, the test statistic (e.g. *F*, *t*, *r*) with confidence intervals, effect sizes, degrees of freedom and *P* value noted *Give P values as exact values whenever suitable.*
☒	☐	For Bayesian analysis, information on the choice of priors and Markov chain Monte Carlo settings
☒	☐	For hierarchical and complex designs, identification of the appropriate level for tests and full reporting of outcomes
☒	☐	Estimates of effect sizes (e.g. Cohen's *d*, Pearson's *r*), indicating how they were calculated

Our web collection on statistics for biologists contains articles on many of the points above.

Software and code

Policy information about availability of computer code

Data collection	Raw MS files were processed with MaxQuant software (version 1.5.2.8).The LTQ Orbitrap Velos was operated in data-dependent acquisition mode with Xcalibur software (version 2.2.SP1.48).
Data analysis	The analysis scripts used for analysis of proteomic data were written in R V3.3 GNU General public licence https://www.r-project.org/ and R studio V1.1.442 GNU General public licence https://www.rstudio.com/ and are available from the corresponding author upon request. For protein network visualization results generated from R scripts were imported in cytoscape V3.3 GNU General public licence http://www.cytoscape.org/. Flow cytometry analysis was performed with FACSDiva software v8 BD FACSDivaTM

For manuscripts utilizing custom algorithms or software that are central to the research but not yet described in published literature, software must be made available to editors/reviewers. We strongly encourage code deposition in a community repository (e.g. GitHub). See the Nature Research guidelines for submitting code & software for further information.

Data

Policy information about availability of data

All manuscripts must include a data availability statement. This statement should provide the following information, where applicable:

- Accession codes, unique identifiers, or web links for publicly available datasets
- A list of figures that have associated raw data
- A description of any restrictions on data availability

The mass spectrometry proteomics data have been deposited to the ProteomeXchange Consortium via the PRIDE partner repository (http://www.ebi.ac.uk/pride) with the dataset identifiers PXD007660 and PXD003972. Figures 1 to 7 are based on raw data. They will be publicly released at the time of publication.

Field-specific reporting

Please select the one below that is the best fit for your research. If you are not sure, read the appropriate sections before making your selection.

☒ Life sciences ☐ Behavioural & social sciences ☐ Ecological, evolutionary & environmental sciences

For a reference copy of the document with all sections, see nature.com/documents/nr-reporting-summary-flat.pdf

Life sciences study design

All studies must disclose on these points even when the disclosure is negative.

Sample size	The sample sizes were chosen from past knowledge on good sample size to ensure adequate power. Sample sizes are always indicated in figure legends or related "Methods" section. Size of samples are defined by the number of mice required to obtain sufficient amount of proteins from primary T cells in accordance with the animal ethical rules. We usually used 6 to 8 mice per group for each experiment related to AP-MS.
Data exclusions	No data were excluded from the analysis
Replication	All experiments were performed at least three times independently and successfully reproduced. Reproducibility of the experiments and significances of the results are described in details in figure legends and in the "Methods" section.
Randomization	No randomization was used given the small number of samples
Blinding	N/A. Given the substantial numbers of cells required for AP-MS (100 X 106 per AP-MS run), cells from several mice of a given genotype (OST or WT) had to be pooled, therefore blinded group assignment cannot be applied.

Reporting for specific materials, systems and methods

We require information from authors about some types of materials, experimental systems and methods used in many studies. Here, indicate whether each material, system or method listed is relevant to your study. If you are not sure if a list item applies to your research, read the appropriate section before selecting a response.

Materials & experimental systems

n/a	Involved in the study
☐	☒ Antibodies
☒	☐ Eukaryotic cell lines
☒	☐ Palaeontology
☐	☒ Animals and other organisms
☒	☐ Human research participants
☒	☐ Clinical data

Methods

n/a	Involved in the study
☒	☐ ChIP-seq
☐	☒ Flow cytometry
☒	☐ MRI-based neuroimaging

Antibodies

Antibodies used	The following antibodies were used for immunoblot analysis: anti-ITK (sc-23902), anti-PTPN6 (sc-287), anti-SHIP1 (sc-8425), and anti-NFATc2 (sc-7296) from Santa Cruz Biotechnology. Anti-PLCG1 (2822), anti-VAV1 (2502), anti-SLP76 (4958), anti-ZAP70 (2705) and anti-LCK (2752) were from Cell Signaling Technology. Anti-THEMIS (PA5-19288) was from Thermo Scientific, anti-NCK1 (610100) was from BD Biosciences, anti-FYB (07-546) was from Millipore and anti-PTPN22 was a gift from Genentech. Whole blood was stained with a combination of eight antibodies from BD Biosciences: peridinin chlorophyll protein-cyanine 5.5-conjugated anti-CD45.2 (104), allophyocyanin-conjugated anti-CD5 (PK136), phycoerythrin-indotricarbocyanine-conjugated anti-CD19 (1D3/6D5), Pacific Blue-conjugated anti-CD4 (RM4-5), Alexa Fluor 700-conjugated anti-CD8α (53.6.7), phycoerythrin-conjugated anti-CD62L (MEL-14), fluroescein isothiocyanate-conjugated CD44 (IM7), and Alexa Fluor 700–conjugated anti–I-A/I-E (M5/114.15.2). Thymocytes and spleen cells from F0 mice were stained with the following antibodies from BD Biosciences: anti-CD5 (53-7.3), anti-CD4 (RM45), anti-CD8 (53-6.7), anti-CD25 (PC61), anti-CD44 (Im7) and anti-CD19 (6D5), and analyzed using an LSRII system (BD Biosciences) and a Diva software (BD Biosciences).
Validation	All the antibodies used in this study are of commercial origin and have been validated by earlier referenced publications and manufacturers

Animals and other organisms

Policy information about studies involving animals; ARRIVE guidelines recommended for reporting animal research

Laboratory animals	All the mouse strains used in this study are on a C57BL/6 background and described in Methods. For experiments, mice were sex matched and were 9 weeks old +/- 1 month.
Wild animals	This study did not involve the use of wild animals.
Field-collected samples	This study did not involve the use of field-collected samples.
Ethics oversight	Mice were maintained in specific pathogen-free conditions and used in accordance with institutional committee and French and European (Marseille) and Chinese (Xinxiang) guidelines for animal care. In vivo procedures were performed in Marseille following protocols approved by the Ethics Committee of Marseille and the Ministry of National Education, Higher Education and Research in accordance with institutional, national, and European directives for animal care (approvals APAFIS 779-2015 0605 10534083 and APAFIS 781-2015 0605 14006182). In vivo procedures were performed in Xinxiang following protocols approved by the Ethics Committee of the Xinxiang Medical School.

Note that full information on the approval of the study protocol must also be provided in the manuscript.

Flow Cytometry

Plots

Confirm that:

☐ The axis labels state the marker and fluorochrome used (e.g. CD4-FITC).

☐ The axis scales are clearly visible. Include numbers along axes only for bottom left plot of group (a 'group' is an analysis of identical markers).

☐ All plots are contour plots with outliers or pseudocolor plots.

☐ A numerical value for number of cells or percentage (with statistics) is provided.

Methodology

Sample preparation	Collect of cells and subsequent sample preparation are described in Methods.
Instrument	MS acquisition was performed with an UltiMate 3000 system (NCS-3500RS Nano/Cap System; Dionex) coupled to an Orbitrap Velos Pro mass spectrometer (Thermo Fisher Scientific). A LSRII system (BD Biosciences) was used for Flow cytometry acquisition.
Software	Flow cytometry analysis was performed with FACSDiva software v8 BD FACSDivaTM
Cell population abundance	Cell population abundance was determined using Trucount tubes (BD Biosciences). Cell viability was evaluated using SYTOX Blue (LifeTechnologies).
Gating strategy	The gating strategy used in the present manuscript is similar to that described in Roncagalli et al Nature Immunolgy 2014; PMID: 24584089)

☐ Tick this box to confirm that a figure exemplifying the gating strategy is provided in the Supplementary Information.